Studies of Coaxial Multipactor in the Presence of a Magnetic Field

by

Gabriel E. Becerra
S.B., Physics
Massachusetts Institute of Technology, 2006

Submitted to the Department of Nuclear Science and Engineering
in partial fulfillment of the requirements for the degrees of

Bachelor of Science and Master of Science
in Nuclear Science and Engineering

at the

MASSACHUSETTS INSTITUTE OF TECHNOLOGY

June 2007

Author .....
Department of Nuclear Science and Engineering
May 25, 2007

Certified by .....
Professor Ian H. Hutchinson
Professor of Nuclear Science and Engineering, Department Head
Thesis Supervisor

Certified by .....
Doctor Stephen J. Wukitch
Principal Research Scientist, Plasma Science and Fusion Center
Thesis Reader

Accepted by .....
Professor Jeffrey A. Coderre
Chairman, Department Committee on Graduate Students

Studies of Coaxial Multipactor in the Presence of a Magnetic Field

by

Gabriel E. Becerra

Submitted to the Department of Nuclear Science and Engineering
on May 25, 2007 in partial fulfillment of the requirements for the
degrees of Bachelor of Science and Master of Science
in Nuclear Science and Engineering

Abstract

Multipactor discharges consists of electron multiplication between two surfaces by secondary electron emission in resonance with an alternating electric field. They are detrimental to the performance of radio frequency (RF) systems, such as the ICRF (ion cyclotron range of frequencies) antennas for heating of plasmas in the Alcator C-Mod tokamak and other nuclear fusion devices.

This work investigates multipactor discharges in the coaxial geometry in the presence of a constant and uniform magnetic field transverse to the direction of electromagnetic wave propagation. Studies on the Coaxial Multipactor Experiment (CMX) show that the magnetic field decreases the degree to which the discharge detunes the RF circuit. However, it enhances the susceptibility of the system to multipactor-induced gas breakdown at low pressures, which appears to cause the observed neutral pressure limits on antenna performance in Alcator C-Mod.

Different surface treatment methods involving roughening and in-situ cleaning failed to suppress the multipactor discharges in a consistent and reliable way in experiments on CMX, despite the success of similar techniques in the parallel-plate geometry.

Electron trajectories are significantly more complicated in the presence of magnetic fields of different strengths, as shown by a three-dimensional particle-tracking simulation using Monte Carlo sampling techniques. The

trends in electron path length, time of flight, impact energy, secondary emission yield and population growth do not account for the experimental observations between the low and high field limits. These appear to be better explained by collective effects not included in the simulations, such as the effect of the magnetic field on charged particle diffusion.

Thesis Supervisor: Ian H. Hutchinson
Title: Professor of Nuclear Science and Engineering, Department Head

Thesis Reader: Stephen J. Wukitch
Title: Principal Research Scientist, Plasma Science and Fusion Center

Acknowledgements

My deepest appreciation and gratitude goes to all those people who have helped and taught me in so many different ways throughout and beyond this work.

First, many thanks to Professor Ian Hutchinson and Steve Wukitch, for their supervision, feedback and understanding. Their support, discussions and encouragement have been driving forces behind the present work.

Also, I would like to thank Tim Graves for introducing me to the field, instructing me in the subtleties of CMX, answering my questions and teaching me to explore different paths on my way here. I am also very grateful to Paul Schmit, who deserves much credit for the development of the simulation code and the CMX upgrade, and who had great initiative during his stay.

Many thanks as well to the PSFC technical and engineering staff for their assistance with the experimental work, especially to Ed Fitzgerald, Andy Pfeiffer, Tommy Toland and Alan Binus. The same goes to the NSE and PSFC administrative staff for their help with dealing with the inevitable bureaucracy, in particular to Clare Egan, Corrinne Fogg, Valerie Censabella and Dragana Zubcevic. I would also like to thank Dr. Anthony Garratt-Reed and the Center for Materials Science and Engineering for the training in SEM microscopy and the availability of their resources.

I would like to thank my family, and my parents in particular, for their unrelenting support, caring and love: I would be nothing without you, and I cannot tell you how much you mean to me. And thanks to Andrés, Lizzy and Ali, for making sure that this is not complete gibberish to the uninitiated, and even giving some very useful insight helping me to understand it myself.

To them and to all those other friends who helped me not only endure but also enjoy these five years here, thank you so much, just for being there. I will miss you more than I know.

Contents

List of Figures

Symbols and Abbreviations

a	inner coaxial conductor radius
b	outer coaxial conductor radius
B_0	external magnetic field strength
c	speed of light in vacuum
d	parallel-plate separation distance
e	elementary charge, $+1.609 \times 10^{-19}$ coulombs
E_0	electric field amplitude (at outer electrode for coaxial geometry)
E_1	first crossover energy
E_2	second crossover energy
E_F	Fermi energy
$E_{\max}$	primary impact energy for maximum δ
E_p	primary electron impact energy
E_s	secondary electron emission energy
f	RF frequency
ICRF	ion cyclotron range of frequencies
k	ratio of electron's impact speed to emission speed
k_{se}, $k_{s\delta}$	surface smoothness factors
k_z	RF wave number

m_e	electron mass, 9.109×10^{-31} kilograms
N	multipactor odd-order
RF	radio frequency
t_0	time of emission of initial electron
V_0	voltage amplitude (defined in Eqs. 2.8, 2.13 for each geometry)
v_0	electron emission speed
v_f	electron impact speed
Z_0	characteristic transmission line impedance
δ	secondary emission yield
δ_{eff}	effective secondary emission yield
δ_{max}	maximum secondary emission yield
ϵ_0	permittivity of free space
η_0	intrinsic impedance in vacuum ($\equiv \sqrt{\frac{\mu_0}{\epsilon_0}}$)
θ	primary electron incidence angle
θ_s	secondary electron emission angle
μ_0	permeability of free space
τ_m	multipactor rise time
τ_{RF}	RF period
Φ	work function
ω	RF angular frequency

Chapter 1

Introduction

Multipactor discharges adversely affect the performance of antennas for plasma heating in nuclear fusion devices such as tokamaks. They consist of electron multiplication between two surfaces driven by secondary electron emission in resonance with an alternating electric field [1, 2]. This effect detunes the circuit of interest in radio frequency (RF) systems, leading to less efficient transfer of energy to the plasma and increased reflected power, which can in turn damage the power source. Other RF components such as vacuum windows can also be damaged by excess heat produced by this phenomenon. More detrimental, however, is the induction of a glow discharge at gas pressures an order of magnitude lower than expected, which appears to be the cause of the consistent antenna failure observed in the Alcator C-Mod tokamak at low pressures [3].

The present work is aimed at obtaining a better understanding of these discharges in configurations relevant to ICRF (ion cyclotron range of frequencies) antennas in tokamaks and other magnetic confinement fusion devices,

and at exploring possible alternatives to avoid this phenomenon. These studies thus concentrate on the coaxial transmission line geometry, for which the open literature is limited, and considers the effect of a uniform and constant externally applied magnetic field transverse to the direction in which the guided electromagnetic waves propagate. This approximates the tokamak magnetic fields as measured in the vacuum sections of the transmission line of an ICRF antenna.

Chapter 2 introduces the subjects of transmission of electromagnetic waves in RF systems (as relevant to ICRF heating antennas in magnetic confinement fusion devices) and secondary electron emission, the process behind electron population growth in multipactor discharges. The understanding of these background topics is then applied in Chapter 3, which reviews the state of multipactor theory in both the parallel-plate and coaxial geometries. The latter is of most interest in practice, but the former is much better understood due to its mathematical simplicity, and provides good insight applicable to the coaxial configuration. This chapter also considers the case of multipactor discharges in the presence of an external magnetic field.

The Coaxial Multipactor Experiment (CMX), designed to study these discharges under controlled conditions, was upgraded by installing magnet coils to simulate the effect of the tokamak fields on the ICRF systems. The setup and the experimental results obtained from CMX are presented in Chapter 4.

A three-dimensional electron-tracking code applying Monte Carlo sampling techniques was also developed to study the effects of magnetic fields on multipactor discharges in the coaxial geometry, mostly in terms of particle

trajectories and multiplication properties. Chapter 5 reviews the structure and results of the simulation, as well as its limitations.

Finally, Chapter 6 discusses the conclusions derived from this work and suggests directions for future work in the field.

Chapter 2

Background subjects

This chapter reviews the foundations for understanding multipactor discharges in the regimes of interest. The first section introduces ICRF heating of plasmas in magnetic fusion devices and in the Alcator C-Mod tokamak in particular, as well as radio-frequency transmission of electromagnetic waves in two important geometries, as applicable to ICRF systems. This is followed by a discussion of secondary electron emission, the process that drives electron multiplication in multipactor discharges. The following chapter builds on these background subjects and presents the state of multipactor discharge theory and the effects of this phenomenon on RF systems.

2.1 ICRF heating and RF transmission

2.1.1 ICRF heating

Tokamaks and other magnetic confinement fusion devices require auxiliary heating in the form of radio-frequency power and neutral beam injection to

complement Ohmic heating. The lowest frequency range for RF heating is the ion cyclotron range of frequencies (ICRF). Several ICRF heating scenarios are used routinely in current experiments and are expected to be applied in the ITER reactor [4].

In the cold plasma approximation, in which the thermal particle motion is ignored, Maxwell's equations combined with Ohm's Law reduce to

$$\nabla \times (\nabla \times \mathbf{E}) = \frac{\omega^2}{c^2} \mathbf{K} \cdot \mathbf{E}. \tag{2.1}$$

The dielectric tensor is given by

$$\mathbf{K} = \begin{pmatrix} S & -iD & 0 \\ iD & S & 0 \\ 0 & 0 & P \end{pmatrix} \tag{2.2}$$

where Stix's notation [5] is used to define

$$S \equiv 1 - \sum_s \frac{\omega_{ps}^2}{\omega^2 - \Omega_s^2}, \quad D \equiv -\sum_s \frac{\omega_{ps}^2 \Omega_s}{\omega(\omega^2 - \Omega_s^2)}, \quad P \equiv 1 - \sum_s \frac{\omega_{ps}^2}{\omega^2},$$

with the plasma frequency and cyclotron frequency for species s given by $\omega_{ps}^2 \equiv n_s q_s^2 / m_s \epsilon_0$ and $\Omega_s \equiv q_s B_0 / m_s$, respectively. Here the species has number density n_s, charge q_s and mass m_s.

Assuming that fields vary in space like $\sim \exp(ik_\perp x + ik_\parallel z)$, where $k_\perp$ and $k_\parallel$ are the components of $\mathbf{k}$ perpendicular and parallel to magnetic field $\mathbf{B}_0$, and defining the vector $\mathbf{n} \equiv \frac{c}{\omega}\mathbf{k}$ with magnitude equal to the refractive index

of the medium, Equation 2.1 becomes

$$\begin{pmatrix} S - n^2\cos^2\theta & -iD & n^2\sin\theta\cos\theta \\ iD & S - n^2 & 0 \\ n^2\sin\theta\cos\theta & 0 & P - n^2\sin^2\theta \end{pmatrix} \begin{pmatrix} E_x \\ E_y \\ E_z \end{pmatrix} = 0, \qquad (2.3)$$

where θ is the angle between $\mathbf{n}$ (or $\mathbf{k}$) and $\mathbf{B}_0$. Non-trivial solutions exist only if the determinant of the matrix vanishes.

In the ICRF range, $\omega^2 \approx \Omega_i^2 \ll \omega_{pe}^2, \Omega_e^2$, where the subscripts i, e correspond to ions and electrons. In this limit, and for a plasma consisting of electrons and a single ion species, the dispersion relation becomes

$$n^2 \approx \frac{\gamma}{1 + \cos^2\theta}, \qquad (2.4)$$

$$n_\parallel^2 = n^2\cos^2\theta \approx \frac{\gamma\Omega_i^2}{\Omega_i^2 - \omega^2}(1 + \cos^2\theta), \qquad (2.5)$$

where $\gamma \equiv \omega_{pi}^2/\Omega_i^2 = 4\pi n_i m_i c^2/B_0^2$. The root given by Equation 2.4 corresponds to the fast magnetosonic (compressional Alfvén) wave; Equation 2.5 is the ion cyclotron (shear Alfvén) wave. The latter is evanescent above the ion cyclotron frequency, which makes it unsuitable for heating in tokamaks. ICRF heating thus depends on the fast wave, which can propagate directly across the magnetic field as long as the cutoff condition $\omega_{pi}^2/\Omega_i(\omega + \Omega_i) > n_\parallel^2$ is satisfied.

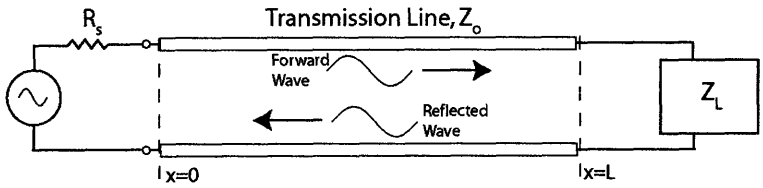

Figure 2.1: RF transmission of electromagnetic waves from a power source to a load via transmission lines. Source: [6].

2.1.2 Radio frequency transmission

Electromagnetic waves are used to deliver power from a radio frequency (RF) source to a load of interest, such as the plasma coupled to the antenna from which the waves are launched for auxiliary heating in tokamaks. The source and the load are connected by transmission lines, discussed in more detail in the Section 2.1.4, as an effective means of transferring the waves with low power attenuation.

The impedances of the source, transmission line and load determine the amplitudes of the forward and reflected waves, as shown in the schematic in Figure 2.1. The reflection coefficient Γ, defined as the ratio of the reflected voltage to the forward voltage, is minimized when the relevant impedances are matched appropriately. Ideally, the line and load impedances are equal, such that the power is delivered without loss to the load and the reflection coefficient vanishes.

However, load impedances cannot usually be set externally to match the source and line impedances. In these cases, an impedance matching network can be used to alter the standing wave pattern so that the reflected power to the source is minimized and most of the forward power circulates in the unmatched side, as illustrated in Figure 2.2.

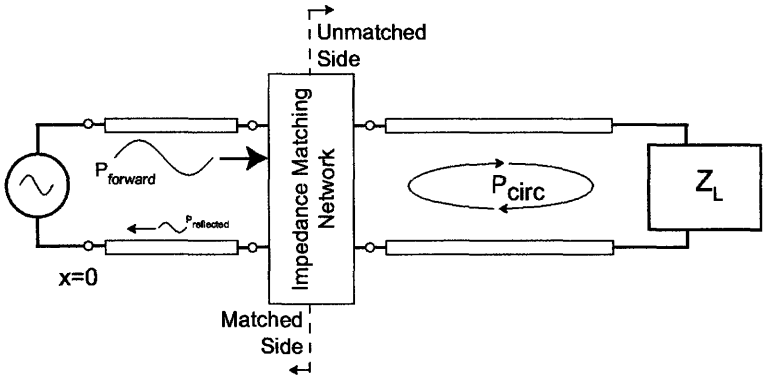

Figure 2.2: Impedance matching for RF transmission. Source: [6].

2.1.3 Alcator C-Mod ICRF systems

The Alcator C-Mod tokamak relies on ICRF heating antenna systems mounted on the D, E and J ports around the outer side of the torus. The first two are two-strap systems with a fixed dipole phase, with end-fed center-grounded current straps and 30 Ω strip line vacuum transmission lines where $\mathbf{E}_{\mathrm{RF}} \perp \mathbf{B}_{\mathrm{tokamak}}$; the J antenna has a compact four-strap configuration with folded straps and a vacuum transmission line combining a 4-inch coaxial line and a parallel-plate one [7].

Figure 2.3 shows a general schematic for each of the antenna systems. An impedance matching network, consisting of a stub tuner and a phase shifter pair, is used in each case to minimize the reflected power to the source. RF vacuum feedthroughs connect the external transmission line to the vacuum transmission lines. Both the vacuum sections of the feedthroughs and the strip line/parallel-plate transmission lines are susceptible to multipactor. However, as will be discussed later, the coaxial sections of the feedthroughs are of greater interest, especially in the presence of the tokamak magnetic

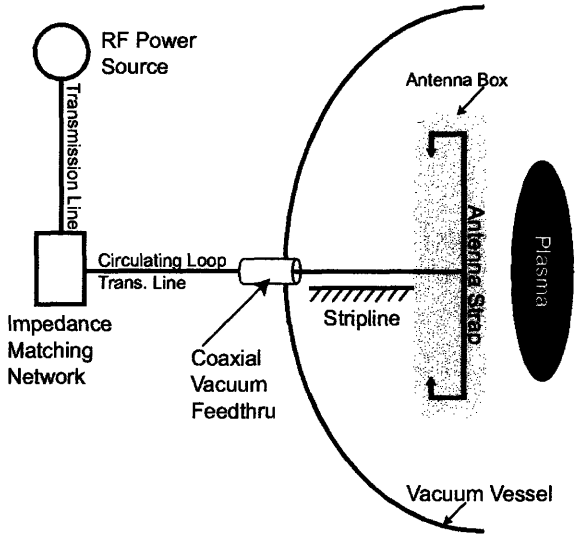

Figure 2.3: Schematic of Alcator C-Mod ICRF heating antenna systems. Source: [6].

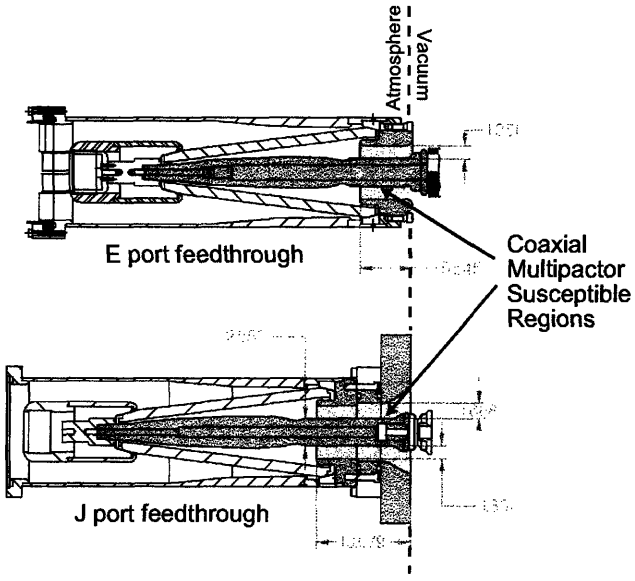

Figure 2.4: RF vacuum feedthroughs. Source: [6].

field, which can suppress multipactor altogether in the parallel-plate geometry. Figure 2.4 shows the structure of the feedthroughs on the E and J ports.

2.1.4 Transmission lines

Transmission lines are used to guide electromagnetic waves from a radio-frequency source to an antenna, from where the waves are launched into the load of interest, such as the plasma in a magnetic fusion device for heating purposes. Usually transverse electromagnetic (TEM) waves are used, such that the electric and magnetic fields are perpendicular to the direction of propagation and to each other. A transmission line consists of two conductors parallel to each other, with a uniform dielectric medium in between, in a geometry in which its cross-sectional shape is constant along the direction of propagation.

The two most common configurations are the parallel-plate and circular coaxial transmission lines. Most of the mathematical theory of multipactor discharges is based on the former geometry, as it is simpler due to its uniform electric field at any point along the line. The latter is often more important practically, as it is better suited to contain vacuum sections, but its radially dependent fields make it mathematically more complicated.

Parallel-plate transmission lines

In this geometry, two identical parallel plates of width w and length ℓ are separated by distance d as shown in Figure 2.5, with the guided wave propagating in the $\hat{\mathbf{z}}$ direction. Typically $d \ll w, \ell$ such that the fields can be

assumed to be confined by the plates and any fringing fields can be ignored.

Assuming vacuum conditions between the plates, the electromagnetic fields vary sinusoidally in time and along the direction of propagation:

$$\mathbf{E}(z,t) = \hat{\mathbf{x}} E_0 \sin(k_z z - \omega t + \alpha), \tag{2.6}$$

$$\mathbf{B}(z,t) = \hat{\mathbf{y}} \frac{E_0}{c} \sin(k_z z - \omega t + \alpha), \tag{2.7}$$

where E_0 is the electric field amplitude, ω is the angular frequency, k_z is the wavenumber, c is the speed of light in vacuum and α is some arbitrary phase.

For a given point along the line, the fields depend purely on time and a potential difference or voltage can be defined as follows by a simple choice of the z and t origins:

$$V(t) = \underbrace{E_0 d}_{\equiv V_0} \sin \omega t. \tag{2.8}$$

For ICRF frequencies, the wavelengths are so large that the voltage variation can be neglected for short enough sections near the point in the line where the amplitude is maximum.

By Ampère's Law, the corresponding current is given by

$$I(t) = E_0 w \sqrt{\frac{\epsilon_0}{\mu_0}} \sin \omega t, \tag{2.9}$$

where ϵ_0 and μ_0 are the permittivity and permeability of free space, respectively. The characteristic impedance of the transmission line is thus

$$Z_0 \equiv \frac{V}{I} = \eta_0 \frac{d}{w}, \tag{2.10}$$

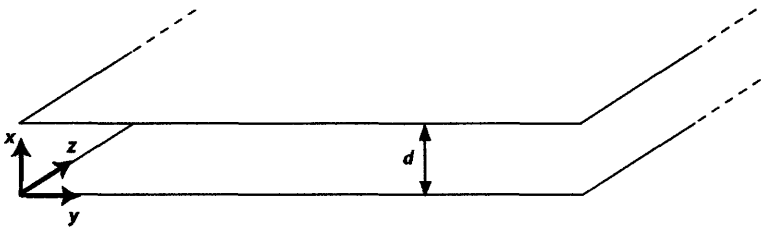

Figure 2.5: Parallel-plate geometry.

where $\eta_0 \equiv \sqrt{\frac{\mu_0}{\epsilon_0}}$ is the intrinsic impedance in vacuum.

Circular coaxial transmission lines

A circular coaxial transmission line consists of an inner cylindrical conductor of radius a and an outer one of radius b, as illustrated by Figure 2.6. The fields in the vacuum between the coaxial electrodes vary like $\sim 1/r$:

$$\mathbf{E}(r,z,t) = \hat{\mathbf{r}} E_0 \frac{b}{r} \sin(kz - \omega t + \alpha), \tag{2.11}$$

$$\mathbf{B}(r,z,t) = \hat{\phi} \frac{E_0 b}{cr} \sin(kz - \omega t + \alpha), \tag{2.12}$$

where E_0 is the electric field amplitude at the outer electrode.

As in the parallel-plate case, a voltage and current can be defined for any point along the transmission line, as follows:

$$V(t) = \underbrace{E_0 b \ln\left(\frac{b}{a}\right)}_{\equiv V_0} \sin\omega t, \tag{2.13}$$

$$I(t) = 2\pi \frac{E_0 b}{\eta_0} \sin\omega t, \tag{2.14}$$

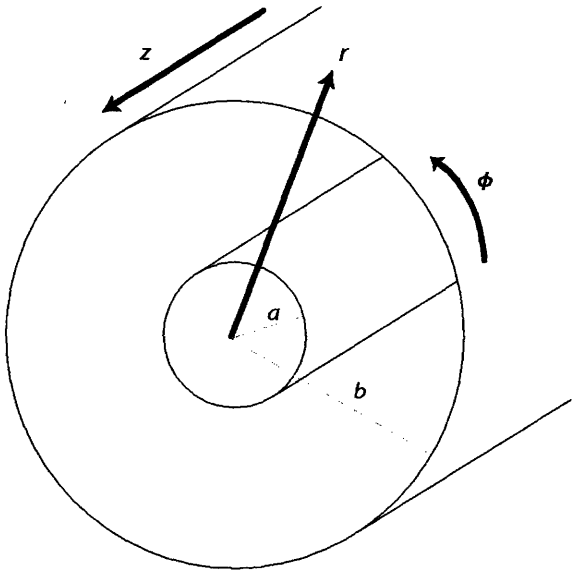

Figure 2.6: Circular coaxial geometry.

such that the line's characteristic impedance is given by

$$Z_0 = \frac{\eta_0}{2\pi} \ln\left(\frac{b}{a}\right). \tag{2.15}$$

The results from the Coaxial Multipactor Experiment to be discussed in the following chapters correspond to $Z_0 = 50\,\Omega$, to match the impedance of the source.

2.2 Secondary electron emission

The impact of an incident ("primary") electron on a surface can lead to the emission of one or more "secondary" electrons from the material. For this study, the surface of interest is one of the transmission line metallic electrodes. The process consists of three main steps:

1. The primary electron crosses the surface of interest and is attenuated by collisions within the material and absorbed.

2. The energy lost by the primary is transferred to electrons inside the material.

3. Some of the excited electrons move toward the surface and are attenuated on their way out by collisions. Those with enough energy to escape the material are secondary electrons and typically have much lower energies than the primary.

Primaries can also be elastically or inelastically reflected; these are not included in the bulk of this study, but a discussion of their effect for the cases of interest is included in Section 2.2.6.

2.2.1 Emission energy distribution

The distribution of the secondary electron emission energies is non-Maxwellian and largely independent of the primary electron energy [8]. It has been approximated by Chung and Everhart [9] as

$$f(E_s) \sim \frac{E_s}{(E_s + \Phi)^4}, \tag{2.16}$$

where E_s is the emission energy of the secondary electron and Φ is the work function of the material*. The most probable value of the secondary energy is given by

$$E_{s,\max} = \frac{\Phi}{3}. \tag{2.17}$$

This distribution is illustrated by Figure 2.7, which also shows a Maxwellian distribution with the same $E_{s,\max}$ for reference.

Adopting a somewhat arbitrary convention [10, 11, 12, 13], the distribution is limited to energies below 50 eV, corresponding to "true" secondaries, i.e. electrons liberated from the material due to the primary impact, not backscattered primaries.

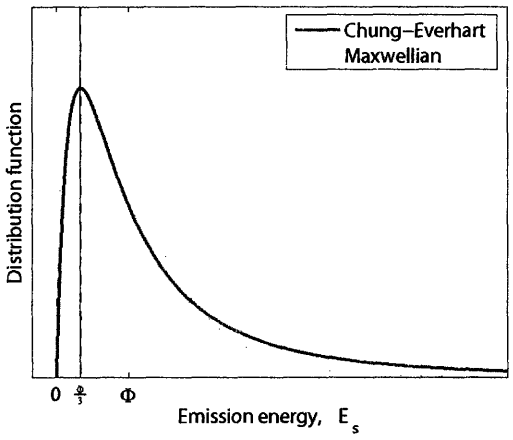

Figure 2.7: Emission energy distribution, as approximated by Chung and Everhart, and by a Maxwellian.

*Chung and Everhart's paper gives the equation in the form $f(E) \sim \frac{E-E_F-\Phi}{(E-E_F)^4}$, where E is the energy measured from the bottom of the metal's conduction band and E_F is the Fermi energy. The emission energy E_s is thus equal to $E - E_F - \Phi$.

2.2.2 Emission angle distribution

The secondary electrons are emitted with an approximate cosine emission angle distribution $f(\theta_s) \sim \cos\theta_s$, with respect to the normal to the surface [10]. This distribution is nearly independent of the incidence angle of the primaries, and assumes a polycrystalline or amorphous surface. Secondaries from single-crystal lattices, on the other hand, are emitted with distributions skewed strongly toward particular angles.

2.2.3 Secondary emission yield

The secondary emission yield or secondary emission coefficient δ is defined as the mean number of secondary electrons emitted per incident primary. It is a function of the energy and the angle of incidence of the primary electrons, and it must be greater than unity for electron multiplication to be possible for a statistically significant number of impacts.

For a given incidence angle, $\delta(E_p)$ should vanish below a threshold primary energy E_0, increase at low energies (as primaries have some energy to transfer to the secondaries), reach a maximum, and decay at larger energies (as very fast primaries penetrate more deeply into the material and more of the excited electrons are stopped before they can reach the surface). This is indeed the case as has been shown experimentally, and secondary electron yield curves are usually identified by the maximum value $\delta_{\max}$ and the primary energy at which the peak occurs, $E_{\max}$, as tabulated for different materials at normal incidence in Table 2.1. The table also includes values for $E_1 < E_{\max}$ and $E_2 > E_{\max}$, the energies at which $\delta = 1$, known as the

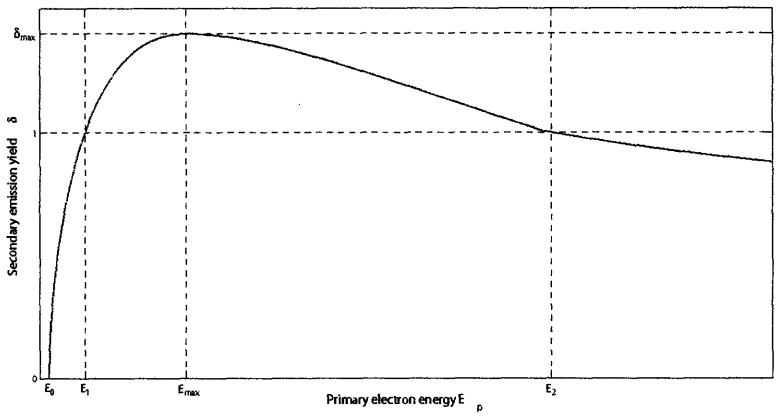

Figure 2.8: Secondary emission yield curve and main characteristics.

first and second crossover points. Clearly, the primary energy must lie between these two energies for there to be more secondary electrons emitted than primaries absorbed, which is crucial for a multipactor discharge to be sustainable. Figure 2.8 illustrates the main characteristics of the secondary electron yield curve $\delta(E_p)$ at a fixed incidence angle.

Since the secondary yield curves consistently show very similar shapes for most materials, a number of different formulas derived theoretically and/or empirically are used in the literature to approximate a "universal" curve, in terms of the parameters discussed in the previous paragraph. Figure 2.9 shows the resulting plots for a few of these formulas, using the same values for $E_{\max}$ and $\delta_{\max}$ in each case.

Vaughan's empirical fit [22, 23] is the most appropriate formula for computational purposes in terms of simplicity and agreement with experiments.

Material	δ_{max}	E_{max}	E_1 (eV)	E_2 (eV)	Source
Cu (cleaned)	1.1–1.3	500–650	200–250	1700	[10, 11, 13, 14]
Cu (baked, 350°C)	1.4	500	130	2150	[14]
Cu (baked, 100°C)	2.1	350–400	< 100	> 3000	[14]
Cu (as received)	2.5	300	< 100	> 3000	[14]
Cu_2O	1.19–1.25	400–440	-	-	[11, 13, 15]
C (soot)	0.45	500	n/a	n/a	[10, 11]
C (graphite)	1.02	300	250	350	[10, 11]
C (diamond)	2.8	750	-	-	[11]
Ti (cleaned)	0.7–0.9	280–300	n/a	n/a	[11, 13, 16]
Ti (as received)	2.0	200	< 100	1500	[17]
Iron	1.1–1.3	200–400	120	1400	[10, 11, 13]
Stainless steel	1.2	400	150–200	1000–1050	[16]
Nickel	1.0–1.35	450–550	140	1100	[10, 11, 13]
Molybdenum	1.0–1.2	350–400	140–200	1000–1100	[11, 13, 16]

Table 2.1: Secondary emission parameters for smooth surfaces of different materials at normal primary incidence.

For $E_p > E_0$, it is given by

$$\frac{\delta(E_p)}{\delta_{max}} = \begin{cases} (\xi e^{1-\xi})^k, & \text{if } \xi \leq 3.6 \\ 1.125/\xi^{0.35}, & \text{if } \xi > 3.6 \end{cases}, \tag{2.18}$$

where ξ and k are given by

$$\xi \equiv \frac{E_p - E_0}{E_{max} - E_0};$$

$$k = \begin{cases} k_1 \equiv 0.56, & \text{if } \xi < 1 \\ k_2 \equiv 0.25, & \text{if } 1 < \xi \leq 3.6 \end{cases}.$$

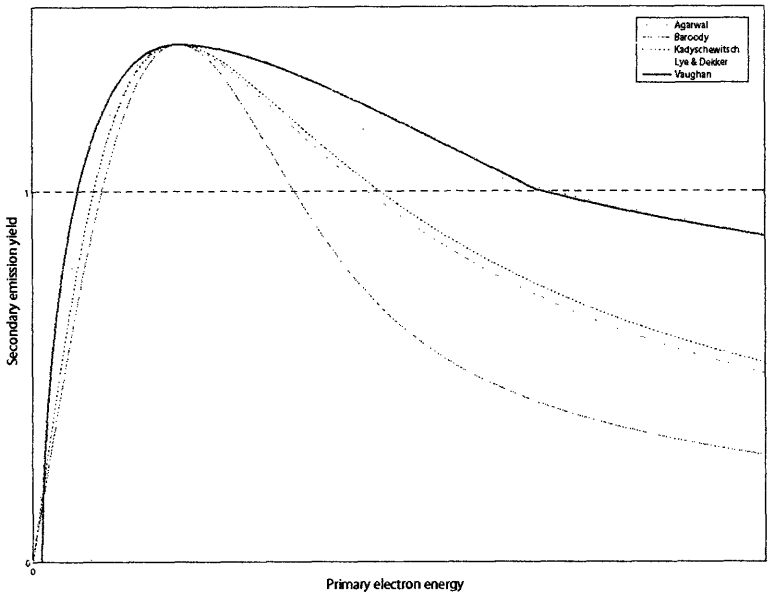

Figure 2.9: Comparison of δ versus E_p curves using the formulas by Agarwal [18], Baroody [19], Kadyschewitsch [20], Lye and Dekker [21] and Vaughan [22, 23].

Effect of oblique incidence

As illustrated in Figure 2.10, when a primary electron is incident at an oblique angle to the surface, it is essentially attenuated in the same way as a primary incident normal to the interface, penetrating the same mean distance x_m into the material. However, the excited electrons are initially closer to the surface, so more of these can leave the material before being stopped on their way out. For an angle θ with respect to the normal, the mean depth changes by a factor $\cos\theta$, thus increasing the secondary yield. Such an increase has been observed experimentally very clearly [24, 25, 26].

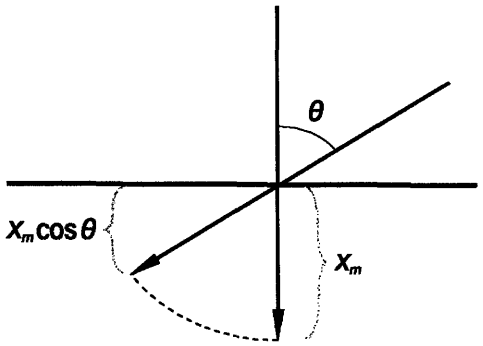

Figure 2.10: Oblique incidence leads to a change in the mean penetration depth by a factor of $\cos\theta$, which makes absorption of excited electrons on their way out less likely, thus increasing the secondary emission yield.

While approaches by Bronshtein and Dolinin [27] and, more reasonably, Bruining [10] conclude that oblique incidence leads to an increase of the yield by a constant factor, experiments by Shih and Hor [28] support Vaughan's empirical formulation [22, 23], according to which both $\delta_{\max}$ and $E_{\max}$ increase with incidence angle, while retaining the overall yield curve shape. Vaughan's formulas for oblique incidence corrections are

$$E_{\max}(\theta) = E_{\max}(0)\left(1 + \frac{k_{se}\theta^2}{\pi}\right) \tag{2.19}$$

and

$$\delta_{\max}(\theta) = \delta_{\max}(0)\left(1 + \frac{k_{s\delta}\theta^2}{\pi}\right), \tag{2.20}$$

where k_{se} and $k_{s\delta}$ are separate smoothness factors for E_p and δ, ranging from 0 to about 2.0, with a default value of 1.0 for typical surfaces. Low values correspond to deliberately roughened surfaces, while high ones are appropriate for very smooth and oxide-free surfaces.

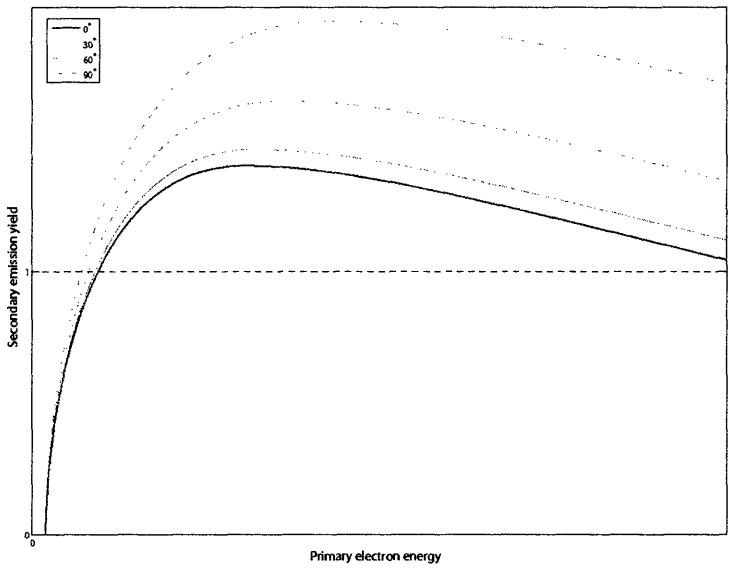

Figure 2.11: Vaughan's secondary emission yield curves for different angles of primary incidence.

Figure 2.11 shows the effect of primary incidence at different angles on the secondary yield curves. Clearly, oblique incidence does not only raise $\delta_{\max}$ and $E_{\max}$, but it also decreases E_1 and increases E_2, thus widening the range for which $\delta > 1$ and making electron multiplication, critical for multipactor onset, more likely.

Oblique incidence is of greater importance in the presence of external magnetic fields, which can therefore increase the effective secondary yield considerably. The extent to which a magnetic field induces more oblique primary incidence is studied later in the present work.

Effect of surface structure

Rough surfaces usually have smaller secondary emission yields than smoother ones, as can be seen from the yield parameters for different variations of carbon in Table 2.1. This is because peaks surrounding the point of emission of a secondary subtend a greater solid angle, thus increasing the likelihood of reabsorption of the electron by one of the peaks, especially for emission at the "valleys" of the surface. However, this is only valid in practice for very clean surfaces, since gases and impurities with higher secondary yields are adsorbed more strongly by rough surfaces, thus increasing the overall yield significantly if they are not removed. The change in δ due to adsorbed impurities can be of up to $\sim$0.5, with the effect being more important at lower primary energies, depending on the secondary yield characteristics of the substances [10].

At the same time, the incidence angle is not properly defined for rough surfaces, so the effect of oblique incidence is essentially negligible for such cases [29]. The smoothness factors in Equations 2.19 and 2.20 reflect this, as a very rough surface corresponds to $k_{se} = k_{s\delta} = 0$ and no incidence angle effect.

Effective secondary yield

An effective secondary electron yield δ_{eff} is sometimes defined [30] for a particular discharge as the ratio of the total number of secondary electrons emitted to the total number of incident electrons. Unlike δ, which gives a statistical expectation that is a function of the energy and incidence angle of primary electrons for a given surface, δ_{eff} is an overall characteristic of the system

and can evolve in time. Assuming that wall interactions, namely secondary emission and primary absorption, are the only mechanisms of electron generation and loss, a δ_{eff} greater than unity indicates overall electron population growth between the electrodes. This assumption is only valid for vacuum conditions, so that other processes such as ionization of gas molecules by electron impact and recombination can be neglected.

2.2.4 Statistical fluctuations

Evidently, statistical fluctuations exist in the number of secondary electrons released by each incident primary, with the secondary yield only giving an average. The relevant literature often assumes Poisson statistics, with a distribution $f(N) = e^{-\delta}\delta^N/N!$, characterized by a variance equal to the expectation, i.e. $\sigma^2 = \delta$. While this is a good first approximation [31, 32], it has been found that it is not valid over all energy ranges [33], especially for high-energy primaries. Alternative approaches for simulations include binomial [34] and log-normal [35] distributions.

2.2.5 Effect of surface curvature

For a curved surface such as the cylindrical electrodes in coaxial transmission line geometries, its curvature can affect some of its secondary emission characteristics. For the coaxial case, the outer conductor acts as a concave surface relative to the incident electrons, while the inner electrode is convex. The emission angle distribution changes in each case from the approximate cosine described in Section 2.2.2, with less electrons emitted at larger angles for concave surfaces, as excited electrons have to travel longer distances to

reach the surface, thus being more likely to be reabsorbed on its way out; the opposite is true for convex surfaces. The secondary electron yield for a concave surface is therefore smaller than for an otherwise identical convex one, but this is largely due to very large angle emission exclusively, which are not typically significant due to the anisotropic emission distribution. The effective yield δ_{eff} can also be affected in the concave case by decreasing the likelihood of primary impacts at large incidence angles.

However, for the case of interest, the effect of surface curvature can be largely neglected. The mean penetration depth of a primary electron is in the order of nanometers [10, 29, 36], while the radii of curvature of the coaxial electrodes used in this work are in the order of centimeters. The ratio of the former to the latter is approximately that of half a meter to the radius of the Earth, so treating the surfaces as locally flat is appropriate for smooth electrodes.

Nevertheless, the curvature might be important for rough surfaces, since the peaks of a concave rough surface are likely to be less "open" than those of a convex one. This can make the adsorption of impurities stronger and increase the solid angle subtended by peaks neighboring the point of emission, and thus affect its secondary yield.

2.2.6 Effect of reflected primary electrons

A fraction of the electrons emitted from a target surface following incidence by primaries consists of primary electrons themselves, which are either elastically or inelastically reflected instead of being absorbed. For a monoenergetic beam of incident primaries, the emission energy distribution described in Sec-

tion 2.2.1 is altered, with a large peak at the beam energy and an extended continuum at lower energies [11]. The large peak corresponds to elastically reflected primaries having transferred essentially no energy to the lattice; the continuum represents electrons that have undergone inelastic collisions and could have excited secondaries from the material. For high incident energies, the continuum overlaps with the tail of the "true" secondaries and it can be hard to distinguish between them but, as mentioned previously, a 50 eV cutoff is usually used to arbitrarily separate them. For a wide distribution of incident energies, of more interest for this work, there should be no large peaks in the emission energy distribution, but there can be relatively small ones corresponding to maxima in the primary energy distribution.

Reflected primary electrons play no direct role in electron multiplication between two surfaces, so they can be ignored for multipactor discharges under vacuum conditions. Indirectly, reflected primaries can contribute to multiplication by exciting secondaries within the material [37], but these should already be included in the total secondary emission yield curve.

The effect of reflected primaries is more important in the presence of gas at intermediate pressures, since they are usually more energetic than secondaries and can ionize the gas molecules, thus increasing the likelihood of breakdown. Vender, Smith and Boswell ignore inelastically reflected primaries altogether for their gas breakdown simulation [30], claiming them to be considerably less numerous than true secondaries and elastically scattered primaries (amounting to $\sim$20% of the number of true secondaries); on the other hand, Gopinath, Verboncoeur and Birdsall, take 90% of all emitted electrons to be true secondaries (using a 20 eV cutoff), while only 3% are

elastically reflected and 7% are medium energy electrons [38].

Chapter 3

Multipactor discharges

The present chapter builds on the previous one and reviews the theories and experimental observations in the multipactor literature. The first section treats the most familiar scenario of multipactor without externally applied magnetic fields, in both the parallel-plate and circular coaxial configurations, with the former being much easier to model and better understood. The second part considers the case of the discharge in the presence of a constant and uniform magnetic field in each geometry. The last section presents the effects of multipactor discharges on RF systems in general and on tokamak ICRF heating antennas in particular.

3.1 Unmagnetized multipactor

Assuming vacuum conditions and ignoring all collective effects and negligible forces, the motion of electrons due to electromagnetic fields is governed by

the Lorentz force:

$$\frac{\mathrm{d}\mathbf{v}}{\mathrm{d}t} = -\frac{e}{m_e}(\mathbf{E} + \mathbf{v} \times \mathbf{B}), \tag{3.1}$$

where e is the elementary charge and m_e is the electron mass. For the transmission line geometries of interest, the amplitude of the electric field is c times that of the magnetic field, so the magnetic force term can be neglected for non-relativistic electrons. Simulations and measurements in the configurations of interest show very few electrons with velocities above a few percent of c, so ignoring the magnetic force is generally an appropriate approach.

The problem is essentially reduced to one dimension, either by assuming that the electron is "average" in that it is emitted normal to the surface, or by simply ignoring any motion perpendicular to the electric field, since there are no significant transverse forces. The equation of motion is then solved for the initial conditions, namely the time of emission of the electron and its position and velocity in the direction of the field at that time. A second electron is assumed to be launched with similar initial conditions from the opposite electrode.

For electrons with the given initial conditions to contribute to a two-sided multipactor discharge two conditions must be satisfied:

1. There must be synchronism between the impacts and the alternating field, so for the process to be repeated cyclically, the transit times of the "forward" and "backward" electrons have to add up to an integer number of RF periods: $\Delta t_1 + \Delta t_2 = n\tau_{\mathrm{RF}} = 2\pi n/\omega$.

2. For there to be electron multiplication in the gap, the product of the

secondary emission coefficients at the impact energies (and incident angles if transverse motion is not ignored) must be greater than unity: $\delta_1\delta_2 > 1$.

3.1.1 Parallel-plate multipactor

Considering a single electron between two parallel plates at $x = 0$ and $x = d$ in an alternating field $E_x = -E_0 \sin \omega t$, the equation of motion is given by

$$\frac{\mathrm{d}v_x}{\mathrm{d}t} = \frac{\mathrm{d}^2x}{\mathrm{d}t^2} = \frac{eE_0}{m_e} \sin \omega t, \tag{3.2}$$

by setting the time origin as the zero phase of the RF field. The minus sign in the electric field is chosen such that the force is in the positive $\hat{\mathbf{x}}$ direction for a small positive t. The equation can be solved analytically, provided the following initial conditions at the time of electron emission t_0 from one of the electrodes:

$$x(t = t_0) = 0, \tag{3.3}$$

$$v_x(t = t_0) = v_0. \tag{3.4}$$

The velocity and position of the electron is then found by integrating the equation of motion taking the initial conditions into account:

$$v_x(t \geq t_0) = v_0 + \frac{eE_0}{m_e\omega}(\cos \omega t_0 - \cos \omega t), \tag{3.5}$$

$$x(t \geq t_0) = v_0(t - t_0) + \frac{eE_0}{m_e\omega^2}(\sin \omega t_0 - \sin \omega t + (\omega t - \omega t_0) \cos \omega t_0). \tag{3.6}$$

Since the electric field in the parallel-plate geometry is independent of

x, the synchronism condition for multipactor can be simplified by assuming that v_0 is the same for every electron, since in that case the condition becomes that every electron's transit time has to be an odd integer number of RF half-periods. If this is satisfied for the first electron, the second electron automatically satisfies it since its motion would be subject to the same forces in the reverse direction. Similarly, assuming equal angles of incidence, $\delta_1 = \delta_2$, simplifying the multiplication condition to simply $\delta > 1$. Such simplifications would not be possible in the coaxial case due to the field's radial dependence.

Making the assumption that v_0 is consistently the same for all electrons, the synchronism condition becomes $x(t = t_0 + N\pi/\omega; N \text{ odd}) = d$. This reduces Equation 3.6 to

$$d = \frac{N\pi v_0}{\omega} + \frac{eE_0}{m_e\omega^2}(2\sin\omega t_0 + N\pi\cos\omega t_0), \tag{3.7}$$

so the voltage amplitude $V_0 \equiv E_0 d$ is given by

$$V_0 = \frac{m_e}{e}\frac{\omega d(\omega d - N\pi v_0)}{(2\sin\omega t_0 + N\pi\cos\omega t_0)}. \tag{3.8}$$

Given v_0, the minimum V_0 satisfying the synchronism condition is such that the denominator is maximized, which happens when $\omega t_0 = \arctan\frac{2}{N\pi}$, giving

$$V_{0,\min} = \frac{m_e}{e}\frac{\omega d|\omega d - v_0 N\pi|}{(4 + N^2\pi^2)^{1/2}}, \tag{3.9}$$

which is thus the lower boundary for the onset voltage of a multipactor discharge of the mode characterized by the given N, provided v_0 is such that

the condition of electron multiplication upon impact is also satisfied.

The upper boundary for the onset voltage can also be obtained by using the maximum negative value of t_0 such that the emission velocity v_0 is just enough for the electron to overcome the initially retarding field, but this cannot be expressed explicitly in a general closed-form equation.

The impact velocity, obtained by imposing the synchronism condition, is

$$v_f \equiv v_x(t = t_0 + N\pi/\omega) = v_0 + \frac{2eE_0}{m_e\omega}\cos\omega t_0, \tag{3.10}$$

from which the impact energy, using the secondary emission notation, can be calculated as $E_p = \frac{1}{2}m_e v_f^2$. The secondary emission yield at this energy for the angle of incidence of interest must then be greater than unity for multiplication to be possible over a large number of cycles, such that electrons with the given conditions can contribute to the development of multipactor discharges.

Evidently, out of the electrons satisfying the synchronism condition, those emitted at $\omega t_0 \pmod{2\pi} \approx 0$ have greater impact energies and, for materials with a very large second crossover energy*, are more likely to satisfy the multiplication condition. This leads to phase focusing or phase selection, such that the electron population over many cycles is restricted to the phases that satisfy said condition and concentrates around the phases that lead to impact energies around E_{max}. The phase range increases with greater electric field amplitude, as more electrons can reach impact energies high enough for

*This is valid for the experiments in this work, using copper electrodes. As seen in Table 2.1, E_2 for copper surfaces of different characteristics is around a few keV, much larger than the bulk of the electron population for voltage amplitudes in the 100–300 V range.

effective multiplication.

Zero emission velocity

Henneberg, Orthuber and Steudel [39] derived certain conditions for the development of multipactor discharges taking the case of zero emission velocity, i.e. $v_0 = 0$ or, equivalently, $E_s = 0$. This idealized case is convenient for mathematical simplicity, but clearly does not represent the electron population, which in practice would follow an energy distribution approximated by Equation 2.16.

In this case, the synchronism condition in Equation 3.8 becomes

$$V_0 = \frac{m_e}{e} \frac{(\omega d)^2}{(2 \sin \omega t_0 + N\pi \cos \omega t_0)}, \tag{3.11}$$

while the minimum onset voltage reduces to

$$V_{0,\text{min}} = \frac{m_e}{e} \frac{(\omega d)^2}{(4 + N^2\pi^2)^{1/2}}. \tag{3.12}$$

The zero emission velocity case is also the only one for which the maximum onset voltage can be expressed in closed form, since it corresponds to $\omega t_0 = 0$. This gives the so-called "geometrical voltage" [1]:

$$V_{0,\text{max}} = \frac{m_e}{e} \frac{(\omega d)^2}{N\pi}. \tag{3.13}$$

All these relations scale like $V_0 \propto (fd)^2$, where $f \equiv \omega/2\pi$ is the RF frequency in hertz. This scaling law holds well in practice to a first approximation, so multipactor "susceptibility diagrams", illustrating the regions

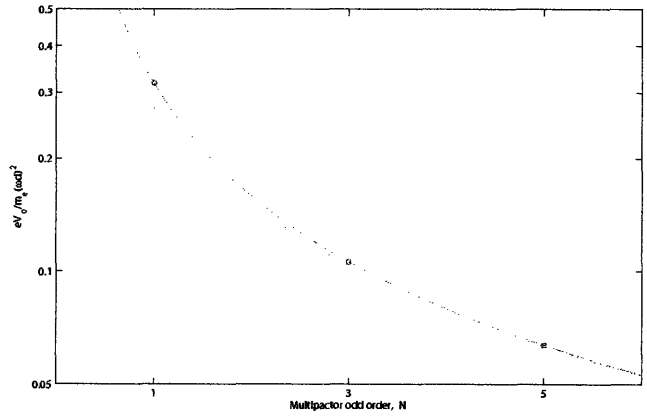

Figure 3.1: Semi-logarithmic plot of the normalized maximum and minimum onset voltage amplitudes as a function of multipactor order N.

where the onset of the discharge is expected, are usually drawn in V_0 versus (fd) plots.

In this limit, it is clear that the voltage requirements for higher order multipactor onset are much more restrictive. As shown in Figure 3.1, the range of onset voltages $\Delta V_0 \equiv V_{0,\max} - V_{0,\min}$ narrows very rapidly with increasing N. Just for the lower orders, $(\Delta V_0)_{N=3} \approx 0.05\,(\Delta V_0)_{N=1}$ and $(\Delta V_0)_{N=5} \approx 0.01\,(\Delta V_0)_{N=1}$. Furthermore, the onset voltage amplitudes within these ranges are lower for higher orders, so the corresponding impact energies are also lower, which usually makes it more difficult for the multiplication condition to be satisfied. The first-order mode is thus usually much more important than all higher modes, and these can often be neglected.

Constant-k theory

Gill and von Engel's assumption that the parameter $k \equiv v_f/v_0$ is constant [40] was retained by Hatch and Williams in their reformulation of multipactor theory [41, 42], which is referred to as the "constant-k" theory and has often been used in the literature [43, 44]. The theory assumes that the value of k only depends on the electrode's material and not on separation, frequency or field amplitude [45]. There is little physical basis for this assumption, as can be seen from Equation 3.10, which clearly shows a dependence on ω and E_0, as well as on the emission phase ωt_0 and v_0 itself, but it leads to some analytical results with reasonable agreement with experiments.

In this theory, the impact velocity can be written as a function of the emission phase only, taking all other variables as external parameters, as

$$v_f = \frac{k}{k-1}\frac{2eE_0}{m_e\omega}\cos\omega t_0, \tag{3.14}$$

while the multipactor onset voltage becomes

$$V_0 = \frac{m_e}{e}\frac{(\omega d)^2}{(\frac{k+1}{k-1}N\pi\cos\omega t_0 + 2\sin\omega t_0)}. \tag{3.15}$$

This is now minimized for $\omega t_0 = \arctan(\frac{k-1}{k+1}\frac{2}{N\pi})$, such that

$$V_{0,\min} = \frac{m_e}{e}\frac{(\omega d)^2}{(4 + [N\pi\frac{k+1}{k-1}]^2)^{1/2}}. \tag{3.16}$$

The equations can be fitted to experimental data to obtain the value of k and the emission phase range leading to multipactor onset. A family of lines can then be obtained to draw a susceptibility diagram, where the breakdown

region is bounded by the lines corresponding to the minimum and maximum emission phases for a given N, and by the lines corresponding to impact energies equal to the crossover energies E_1 and E_2. Good agreement with experiments has been obtained for $k \sim 3$–5.

Computational studies of electron trajectories by Miller, Williams and Theimer [46], as well as a phase-similarity principle for electrons contributing to multipactor discharges introduced by Woo and Ishimaru [47], show that the constant-k assumption is successful, despite being an oversimplification, because only a narrow portion of the distributions in each of v_0 and v_f of the electrons satisfy the synchronism condition, so a constant ratio k is favored for those electrons that do participate in the development of the discharge.

Monoenergetic emission

Modeling using monoenergetic emission has been favored by Vaughan [1] and Krebs and Meerbach [48]. The literature shows several recent examples of the use of this approach over the constant-k theory or the zero emission energy assumption [2, 49, 50]. The physical basis behind this model is stronger than that of the constant-k theory, but this approach does not yield susceptibility diagrams as easily. In any case, a full emission energy distribution is more appropriate for realistic simulations.

Emission energy distribution

The use of full emission energy distributions requires numerical solutions and usually Monte Carlo iterative sampling techniques to adequately approximate the distribution. Results are therefore more statistical and realistic in na-

ture. The Chung-Everhart distribution reviewed in Section 2.2.1 is a good approximation for use in simulations, though the literature also shows choices of Maxwellian and primary-energy-dependent distributions, though these are not as realistic or convenient.

The inclusion of a realistic emission energy distribution has the advantage of allowing for more flexible resonance conditions than those for monoenergetic emission. Otherwise, the conditions for multipactor resonance are very restrictive, with the emission phase as the only degree of freedom.

Growth and saturation

The electron population grows very rapidly after the onset of a multipactor discharge. For a constant effective secondary emission yield $\delta_{\text{eff}} > 1$, the electron population density n_e grows by the square of that value after each RF period (assuming a discharge of order $N = 1$). The population thus grows exponentially with time scale $\tau_m = \frac{\tau_{\text{RF}}}{2 \ln \delta_{\text{eff}}}$. For example, $\delta_{\text{eff}} = 1.2$ corresponds to $\tau_m \sim 2.7 \tau_{\text{RF}}$.

As the electron population increases, several saturation mechanisms start to affect the buildup until a steady-state density is reached. One such mechanism occurs due to space charge effects [1, 49]. Phase focusing occurs over many cycles around the phases allowing electrons to satisfy both the synchronism and multiplication conditions, so the electrons of the same multipactor order can be viewed as a thin sheet of negative charge. Individual electrons are then pushed ahead or behind the sheet by repulsion, especially as the electron population has increased and the sheet charge is large. The defocused electrons are then less likely to satisfy the multipactor conditions, so

many fail to produce new electrons or excite electrons with unfavorable conditions for further multiplication. Moreover, since the sheet thickness is finite, electrons inside the electrode excited by the leading edge of the sheet can experience a strong repulsion from the lagging electrons close to the surface and their emission from the surface can be inhibited.

Kishek and Lau have also presented a model of saturation through the change of the cavity voltage due to the detuning of the RF circuit by the multipactor discharge [51], which assumes a current source. Also, collisions with gas molecules disturb the resonance condition, but this is a minor saturation mechanism at very low pressures.

3.1.2 Coaxial multipactor

The equation of motion for an electron in a coaxial transmission line driven by an electric field $E_r = -E_0 \frac{b}{r} \sin \omega t$ is*

$$\frac{\mathrm{d}v_r}{\mathrm{d}t} = \frac{\mathrm{d}^2 r}{\mathrm{d}t^2} = \frac{eE_0 b}{m_e r} \sin \omega t, \tag{3.17}$$

which cannot be solved analytically due to the r dependence of the electric field, so the geometry is considerably more complicated than the parallel-plate configuration and numeric computation is necessary. Furthermore, secondary electrons emitted at an angle from the outer electrode at high energies can miss the opposite (inner) electrode, which has no equivalent in the parallel-plate case.

*This is the preferred mathematical treatment for an electron emitted from the inner conductor, such that the force is in the positive $\hat{\mathbf{r}}$ direction for small positive t. Conversely, setting the time origin such that $E_r = +E_0 \frac{b}{r} \sin \omega t$ is more convenient for an electron

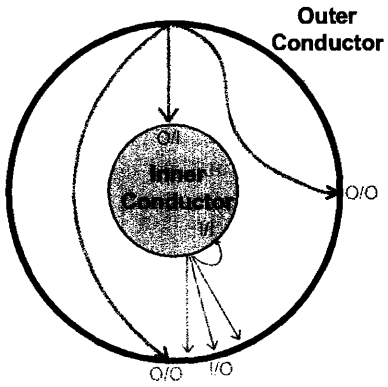

Figure 3.2: Schematic of possible electron trajectories in coaxial multipactor discharges. Source: [6].

There are very few studies of coaxial multipactor discharges in the open literature. Woo and Ishimaru argued for the applicability of their theoretical similarity principle to all geometries allowing for multipactor [47], and Woo studied the coaxial case experimentally [52, 53], finding the principle to hold well. The model gives some legitimacy to the constant-k theory, and both predict the onset voltage boundaries following a $\sim (fd)^2$ dependence, where $d = b - a$, for a given characteristic line impedance Z_0. The experimental agreement is good, except for the lower boundary at low b/a ratios (low Z_0). Woo argues that for $Z_0 \approx 50\,\Omega$ (the case considered experimentally and computationally in the present work), the electric field is relatively uniform spatially and higher-order modes can exist for large fd, which account for the discrepancy. Reducing the secondary yield of the surfaces by outgassing the electrodes is seen to be sufficient to suppress higher-order modes and leads to better agreement with the models. For larger b/a, the field is less uniform

emitted from the outer conductor.

across the gap, which makes higher-order modes difficult.

Udiljak et al. find, through an approximate analytical solution, that one-surface (outer-to-outer) multipactor voltages exhibit a $\sim (fb)^2 Z_0$ dependence [54], in agreement with numerical calculations by Pérez et al. [55] and Somersalo, Ylä-Oijala and Proch [56]. There is no agreement on a simple general scaling law for two-surface discharges: Udiljak et al. favor a $\sim (fd)^2$ scaling, with no Z_0 dependence for the voltage, but only for the $N = 1$ mode, while Somersalo's group suggests $\sim (fb)^2 Z_0^{3/2}$, which is only accurate for the first order mode for high values of b/a.

Electron trajectories can be calculated numerically in one dimension since the force is purely radial and each electron's angular momentum is thus conserved throughout its flight. Graves developed a one-dimensional particle-tracking simulation on this basis and obtained impact energy distribution functions with good agreement with experimentally determined distributions [6]. The shape of such distributions is similar to that of parallel-plate ones for the same electrode separation d (with a coaxial $Z_0 = 50\,\Omega$), frequency, surface material and voltage amplitude. However, the high-energy population peak is consistently located near 80% of the voltage amplitude expressed as the equivalent energy eV_0 for the coaxial geometry, whereas the parallel-plate case shows a peak at a lower energy, around 65–70%. The tail of the distribution is also typically more significant in the coaxial case, with electrons with $E_p > eV_0$ corresponding to outer-to-outer trajectories passing close to the inner conductor.

Udiljak et al. derived an approximate analytical solution to the nonlinear equation of motion for the coaxial case, with very good agreement with

numerical solutions [54]. However, the derivation assumes that $\Lambda \ll (\omega R)^2$, where $\Lambda \equiv eE_0 b/m_e = \frac{e\eta_0}{2\pi m_e Z_0} V_0$ and R is the time-averaged radial position of the electron, distinguished from the fast oscillating motion. This assumption is largely valid for the GHz frequencies considered in their paper, where the right-hand-side is over an order of magnitude larger, but it is not for ICRF frequencies, the range of interest for this work. The results by Udiljak et al. are nevertheless useful overall, and have been confirmed numerically by Semenov et al. [57], who also show that the effects of the emission energy distribution and the surface secondary emission characteristics on coaxial multipactor discharges, both one and two-surface, are very similar to those for the parallel-plate geometry.

3.2 Magnetized multipactor

3.2.1 Parallel-plate multipactor in the presence of a magnetic field

The literature shows several studies of crossed-field multipactor discharges both in metals and dielectrics, significantly affecting the resonance conditions [58, 59, 60]. Simulations and experimental results have shown that multipactor discharges in this geometry can be suppressed in the presence of a constant magnetic field perpendicular to the alternating electric field [61, 62, 63]. The coaxial case is therefore of more interest, since the tokamak fields are large enough to disturb the conditions for multipactor in the parallel-plate components of the ICRF heating antenna systems.

3.2.2 Coaxial multipactor in the presence of a magnetic field

While Equation 3.17 governing the electron motion in a coaxial transmission line cannot be solved analytically, the presence of an externally applied, constant (DC) magnetic field perpendicular to the direction of propagation further complicates the mathematical treatment, by introducing ϕ and z components to the Lorentz force. These non-radial force components also generate torque, so angular momentum is no longer conserved along the electron's trajectory, and three-dimensional numerical solutions are necessary. By defining the coordinates such that the magnetic field is in the $\hat{\mathbf{y}}$ direction, as shown in Figure 3.3, then $\mathbf{B} = \hat{\mathbf{y}}B_0 = \hat{\mathbf{r}}B_0 \sin\phi + \hat{\phi}B_0 \cos\phi$, so that the electron motion is given by

$$\frac{\mathrm{d}v_r}{\mathrm{d}t} = \frac{\mathrm{d}^2 r}{\mathrm{d}t^2} + r\left(\frac{\mathrm{d}\phi}{\mathrm{d}t}\right)^2 = \frac{eE_0 b}{m_e r}\sin\omega t + \frac{eB_0}{m_e}v_z \cos\phi, \tag{3.18}$$

$$\frac{\mathrm{d}v_\phi}{\mathrm{d}t} = 2\frac{\mathrm{d}r}{\mathrm{d}t}\frac{\mathrm{d}\phi}{\mathrm{d}t} + r\frac{\mathrm{d}^2\phi}{\mathrm{d}t^2} = -\frac{eB_0}{m_e}v_z \sin\phi, \tag{3.19}$$

$$\frac{\mathrm{d}v_z}{\mathrm{d}t} = \frac{\mathrm{d}^2 z}{\mathrm{d}t^2} = \frac{eB_0}{m_e}(v_\phi \sin\phi - v_r \cos\phi). \tag{3.20}$$

In the high $\mathbf{B}$-field limit, the electron's motion becomes essentially one-dimensional as it is constrained to the direction parallel to the field. The transverse motion becomes negligible as the electron's Larmor radius $r_L \equiv m_e v_\perp / eB_0$ vanishes, where $v_\perp^2 = v_x^2 + v_z^2 = (v_r \cos\phi - v_\phi \sin\phi)^2 + v_z^2$ is the squared speed transverse to the magnetic field. The parallel motion is thus

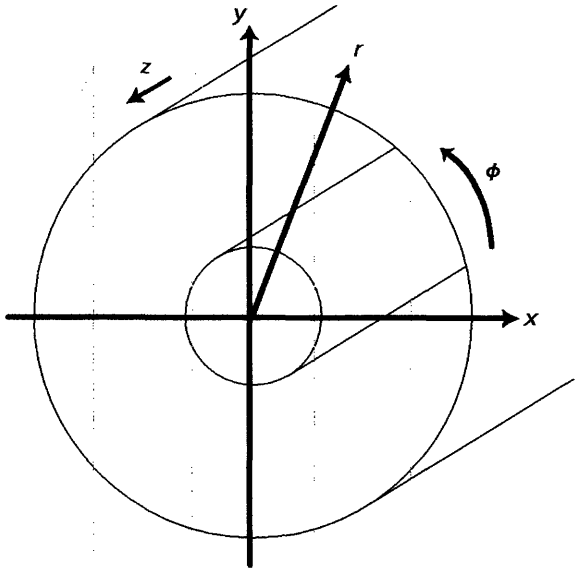

Figure 3.3: Coaxial geometry in the presence of a uniform, DC magnetic field $\mathbf{B} = \hat{\mathbf{y}}B_0$.

driven by the y component of the RF electric field only, so that

$$\frac{\mathrm{d}v_{\parallel}}{\mathrm{d}t} = \frac{\mathrm{d}v_y}{\mathrm{d}t} = \frac{\mathrm{d}^2y}{\mathrm{d}t^2} = \frac{eE_0b}{m_er}\sin\phi\sin\omega t = \frac{eE_0b}{m_e}\frac{y}{(x_0^2+y^2)}\sin\omega t, \qquad (3.21)$$

where x_0 is the electron's x coordinate at emission. For $|x_0| > a$, the electron's trajectory necessarily starts and ends at the outer electrode; otherwise, it will start and end at different surfaces, provided it is energetic enough. For $x_0 = 0$, Equation 3.21 reduces to a mathematical equivalent of Equation 3.17.

3.3 Effect of multipactor discharges on RF systems

Multipactor discharges are known to have many detrimental effects on RF systems. First, they generate excess heat, which can lead to melting, cracking or other damage of components. Second, the discharge effectively makes the transmission line gap a conductive medium and changes the line's impedance, thus detuning the RF circuit. As illustrated in Figure 3.4, this leads to a decrease in the circulating power on the unmatched side and increased reflected power to the RF source. The former implies inefficient transfer of power to the load (the plasma in the case of interest) and the latter can damage the source if large enough.

More relevant to nuclear fusion devices, multipactor can induce gas breakdown at lower gas pressures than those expected by a regular RF Paschen breakdown [64], which appears to be the cause of a consistently observed ICRF antenna failure on the Alcator C-Mod tokamak [6, 3]. The development of a multipactor discharge affects the development of the gas breakdown by increasing both the electron population, via secondary emission from the

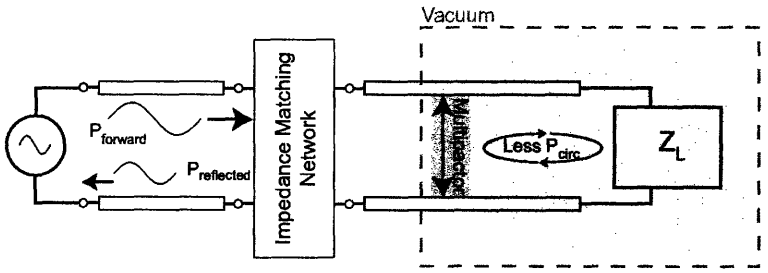

Figure 3.4: Detuning of RF system by multipactor discharge. Source: [6].

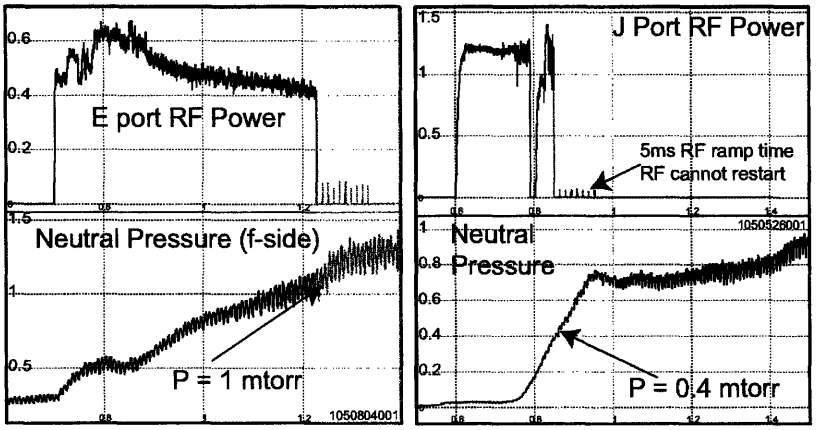

Figure 3.5: Neutral pressure limits observed on Alcator C-Mod ICRF heating antennas at E and J ports. Source: [3].

walls, and the gas density by desorption of gas from the surfaces, thereby increasing the rate of gas ionization by electron impact. This evidently increases the probability of it overcoming any mechanisms of ion and electron loss (such as recombination, attachment and diffusion to the walls), thus leading to an avalanche effect and the development of a glow discharge.

Figure 3.5 shows the experimentally observed neutral pressure limits on the performance of E and J ICRF antennas on Alcator C-Mod. The sharp drops in RF power correspond to approximately 1 and 0.4 millitorr pressures, respectively, as measured from the G port. The sections shaded in yellow show short RF pulses signaling the failure to restart the antennas at pressures beyond those limits. These results were taken during typical operation of the tokamak, with a strong 5.4 T magnetic field at the center (~ 4 T in the antenna region).

Multipactor susceptibility experiments by Graves on the E and J antennas [3] show a large drop in the circulating power at 1 and 0.5 millitorr pressures

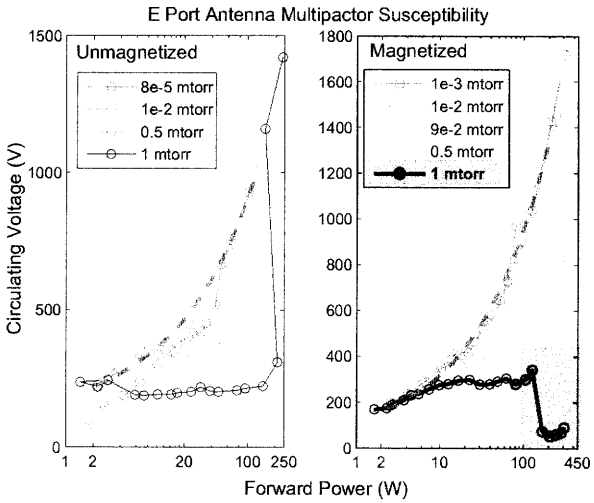

Figure 3.6: E-port C-Mod results. Source: [3].

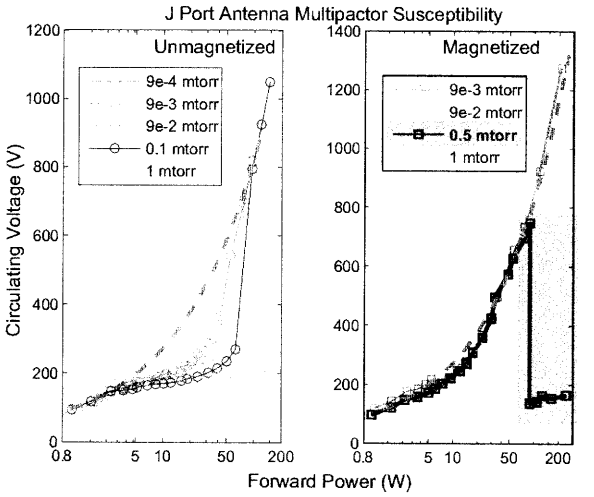

Figure 3.7: J-port C-Mod results. Source: [3].

in the presence of a 0.1 T (1000 G) field, respectively, as shown in Figures 3.6 and 3.7. These correlate well with the neutral pressure limits during regular operation, strongly suggesting multipactor as the reason behind antenna failure at those pressures. The simulations in Chapter 5 show the saturation of most effects of the magnetic field beyond a few hundred gauss, so the similar limits observed in these two scenarios are consistent despite the order of magnitude difference in magnetic field strength.

Chapter 4

Coaxial Multipactor Experiment (CMX)

The experiments described in this work were performed in the Coaxial Multipactor Experiment (CMX), a tabletop setup for the study of multipactor discharges under controlled conditions [6, 65]. In particular, it provides a good platform for investigations in the regimes of interest, as relevant to Alcator C-Mod RF systems. Experiments were carried out to determine the effect of an external magnetic field on multipactor discharges in coaxial transmission lines.

4.1 Setup

While CMX can be set up in both the coaxial and parallel-plate geometries, the results presented here correspond to the former only. The core of the system is a 10-inch, stainless steel vacuum chamber designed to reach ultra

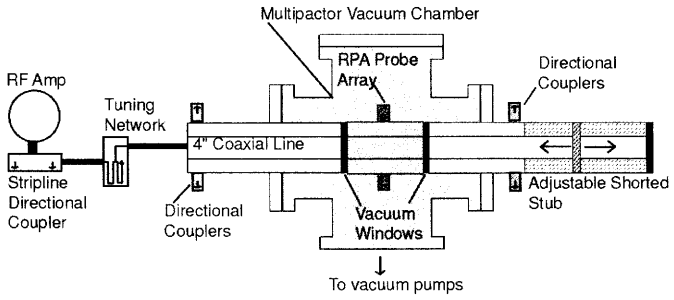

Figure 4.1: CMX coaxial setup schematic. Source: [65].

high vacuum base pressures ($\sim 5 \times 10^{-8}$ torr). Gas, typically argon, is introduced from the top, using a manual gas bleed valve to adjust its pressure. As shown in Figure 4.1, a 4-inch, 50 Ω coaxial transmission line crosses the chamber, with the vacuum section within the line limited to 15 cm by Teflon gas barriers. This section is where the discharges of interest are generated. A shorted stub at the end of the line is adjusted so that it is one quarter-wavelength away from the chamber's center, such that the standing wave pattern's maximum voltage amplitude is located at the center and there is minimal voltage variation within the vacuum section.

A stub tuner and a phase shifter pair act as a tuning network, used to obtain the impedance matching appropriate to the frequency of interest in the 40–150 MHz range, as set by the RF source, so that the reflected power to the source is minimized during multipactor-free operation. A directional coupler pair on the matched side gives the forward and reflected power for the source, while pairs on both sides of the chamber are used for circulating power measurements, from which the voltage amplitude in the vacuum section can be determined. Current measurements for determining electron

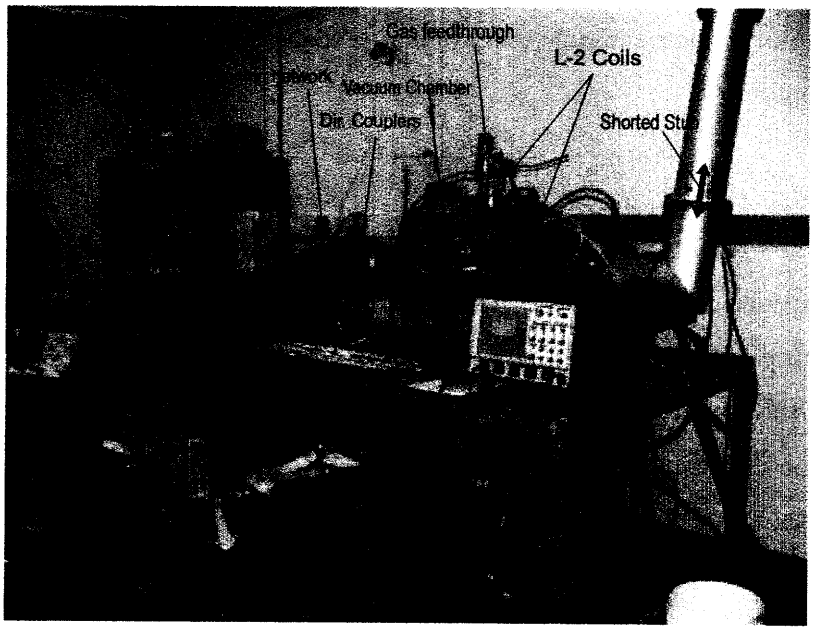

Figure 4.2: Upgraded CMX experimental setup in the coaxial geometry.

impact energy distributions can be made with retarding potential analyzers located around the outer conductor's surface.

The experimental setup was upgraded by installing four water-cooled, 33-turn L-2 coil magnets [66], as shown in Figure 4.2 allowing investigations of multipactor discharges in the presence of a magnetic field across the coaxial transmission line. A pair of magnets are mounted on each side of the chamber in a Helmholtz configuration, capable of generating DC fields of several hundred gauss, as measured at the center of the chamber. The field is close to uniform inside the vacuum section of the transmission line where multipactor discharges are induced. Such a field approximates that in C-Mod's ICRF antenna systems, where the tokamak's toroidal and poloidal fields superimpose such that the resultant field in the multipactor-susceptible

section is approximately uniform and perpendicular to the direction of wave propagation.

4.2 Results

The following experiments were carried out to obtain information on how multipactor discharges and their effects in the coaxial geometry are changed by the presence of a DC, close-to-uniform magnetic field transverse to the direction of propagation of waves. Field strengths of up to 100 G were used. Tokamak-relevant fields are usually in the kilogauss range (typically 1–4 T for Alcator C-Mod), but, as seen from the simulations presented in the following chapter, the effect of the magnetic field largely saturates for large fields, so the results at very high field strengths can be easily induced from those at the higher B_0 in these experiments.

4.2.1 Effect of magnetic field

The introduction of the magnetic field has the overall effect of sharply decreasing the reflection coefficient of the RF system, as measured at the source, for pure (vacuum) multipactor discharges, as can be seen in Figure 4.3. This is consistent with the experimental results from Alcator C-Mod reported by Graves et al., which showed multipactor to be less reactive to the RF circuit in the presence of a magnetic field [6, 3]. The discharge detunes the system less, so it is less likely to lead to damage to the source and other undesirable effects. However, this also means that it is more difficult to detect the discharge, since reflected power measurements are a common method of

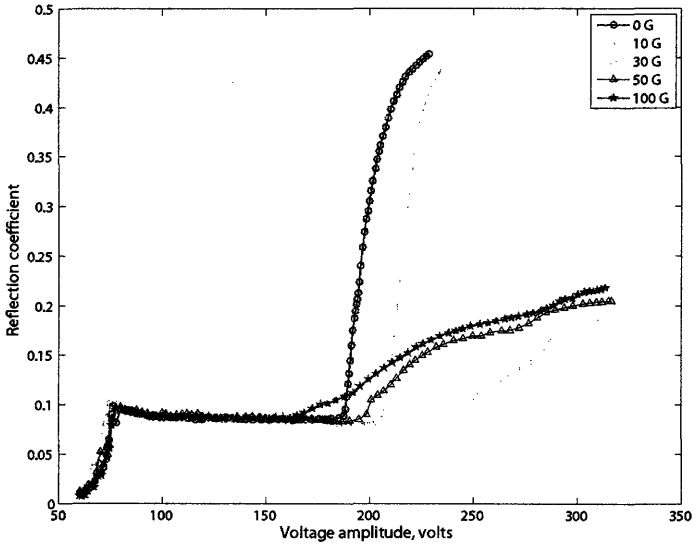

Figure 4.3: Effect of magnetic field on reflection coefficient as measured at the RF source.

multipactor detection.

As discussed in Section 3.3, multipactor discharges detune the systems by changing the transmission line impedance. High magnetic fields constrain the particle trajectories such that the possibility of opposite-electrode impact is restricted to paths with $|x_0| \lesssim a$, as discussed in more detail in the next chapter. The conductivity of the medium due to multipactor discharges is thus less likely to be significant at high magnetic field strengths, which could explain the lesser degree to which the RF circuit is detuned.

This effect alone is enough to illustrate the importance of taking magnetic fields into account during design of RF systems when trying to deal with multipactor discharges. However, the most important effect of the in-

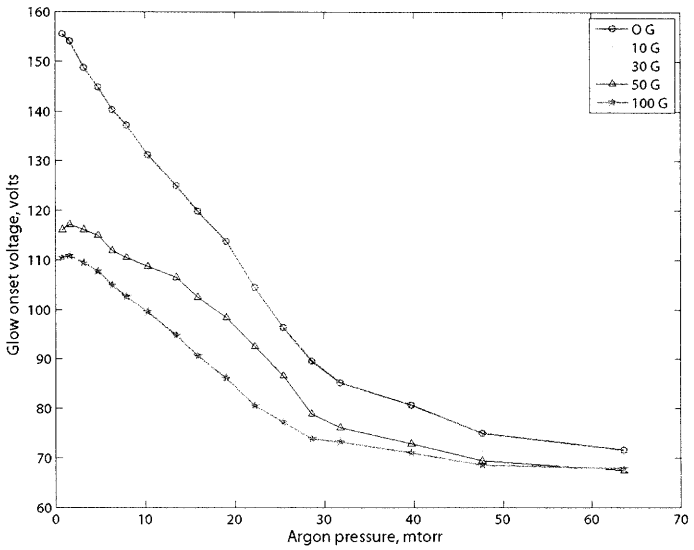

Figure 4.4: Effect of magnetic field on glow discharge onset voltage.

troduction of **B**-fields is the decrease of the lower boundary of onset voltages for glow discharges for pressures in the millitorr range, as seen in Figure 4.4. This effect is stronger for pressures in the multipactor-induced glow range, while there is some degree of convergence in the Paschen breakdown regime. The minimum breakdown neutral pressures at given voltage amplitudes also decrease, which implies worse pressure limitations on antenna performance in tokamaks at high-field operation.

While the most important comparison is between the unmagnetized case and the very high field limit, more relevant to tokamaks, it must be noted that the effect of the magnetic field on both the pure multipactor reflection coefficient and breakdown voltages at low pressures shows non-linear behavior, with the maximum change actually occurring at field strengths in the

order of 30 G.

The single-particle trajectories are very complicated in this field range, as will be discussed in Section 5.2. The gyroradius of the Larmor motion induced by the magnetic field is of the same order as the separation distance between the electrodes, and the mean path length and mean flight time are maximized in this regime, as many electrons near the $y = 0$ plane miss the opposite electrode altogether.

4.2.2 Multipactor avoidance

Multipactor prevention techniques usually fall in one of three categories: geometric fixes, DC biasing and surface treatments [1]. The first are usually the most effective, consisting of changing the geometry of multipactor-susceptible sections such that it is unfavorable for resonance conditions; DC biasing involves suppressing electron motion across a gap by applying a large DC electric field bias between the electrodes. However, both of these are often subject to other engineering constraints, and become considerably more complicated in a coaxial system in the presence of a large magnetic field. On the other hand, surface treatments, designed to lower the secondary emission yield of the surfaces, are less susceptible to these constraints, but can degrade over time.

A surface treatment suggested in [6] for multipactor avoidance was tested in the coaxial geometry. The secondary emission yield is lower for rough surfaces, as explained in Section 2.2.3. In the case of interest, the maximum δ of copper transmission lines as those used in the Alcator C-Mod systems must be reduced below unity for the relevant incoming electron energies in order

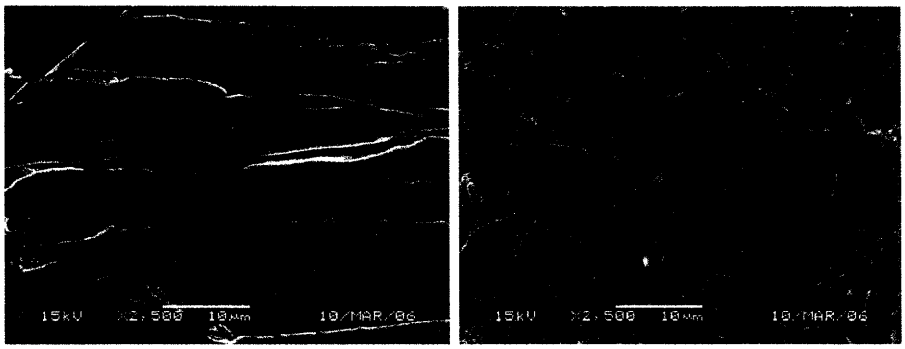

(a) Machined (b) Sandblasted

Figure 4.5: Scanning electron microscope images of different surface structures.

to prevent multipactor discharges altogether. Electron multiplication by secondary emission would be impossible in such a scenario. Roughening the copper electrodes in the parallel-plate configuration of CMX has been shown to suppress multipactor with good high-voltage handling properties [6], which was also tested again for this work. The treatment consists of sandblasting the surfaces with 50 μm aluminum oxide bead (S.S. White Airbrasive Powder, Accubrade©-50, Blend #3). Figure 4.5 shows sample scanning electron microscope (JEOL 5910) images for a surface sandblasted in this fashion and one from a machined surface, more representative of electrodes used routinely in RF vacuum systems, illustrating the degrees of roughness of each.

The sandblasting procedure was repeated for the present work on either the inner or outer conductors of the transmission line, or both. Due to the larger surface area, the surfaces retain more gases and impurities, which increase the overall δ, and must be prepared in situ by glow discharge cleaning

(GDC), baking or long outgassing times.

Unlike the parallel-plate case, GDC was generally unsuccessful in suppressing multipacting. This may be attributed to the low vacuum conductance of the coaxial section; the cleaning process also removed impurities from the Teflon gas barriers, which were not pumped out of the system effectively and were deposited on the electrode surfaces instead, thus preventing any significant decrease in the secondary emission yield of the surfaces. Alternative approaches like changing the windows to a ceramic and trying an open-side configuration of the coaxial section to increase the vacuum conductance of the system were attempted, but failed to lead to a consistently reliable method of multipactor prevention. The options of multipactor conditioning and long-term outgassing were also undesirable considering the time scales needed for these processes.

There were varying degrees of success with eliminating multipactor-induced glows in the open-end coaxial configuration. While pure multipactor was never consistently avoided, glows were often removed at low pressures at which they had routinely appeared before cleaning, at least up to the power levels that the CMX setup allowed for. Even if vacuum multipactor persists, the voltage amplitudes satisfying the resonance condition can be different in the presence of low-pressure gas; also, the multipactor buildup at these pressures might not be sufficiently fast to induce enough ionization to overcome electron loss mechanisms and lead to full gas breakdown.

One partially successful cleaning method consisted of starting the cleaning glow at the RF frequency at which the system was tuned, followed by a change in the frequency after the glow was underway, which did not extinguish it

and could be chosen such that the reflected power was minimized. This increased the circulating power in the system during the cleaning, leading to high temperatures that enhanced the cleaning. However, this also led to sputtering of metallic components that led to plating of components such as the gas barriers.

A variation of this method was following the same procedure in the presence of a strong magnetic field. This typically led to better glow prevention for magnetized operation, but was ineffective in avoiding unmagnetized multipactor-induced breakdown, despite the threshold for the latter usually being higher, as seen in Section 4.2.1. This is because the presence of a **B**-field leads to selective cleaning of the regions of the coaxial section more susceptible to magnetized multipactor, whereas unmagnetized discharges are still likely on the parts of the surface that are not cleaned as well.

Overall, though, no surface treatment method was found to consistently eliminate multipactor discharges, or at least its undesirable effects and low-pressure glow discharges in particular, in a reliable fashion in the coaxial geometry and in the presence of a magnetic field. Some further scanning electron microscope imaging was performed for rough surfaces of different curvatures, followed by stereoscopic imaging analysis, to see if the peak structure in the concave and convex surfaces could have an effect on the inefficiency of the cleaning method in this geometry in particular, but no significant differences were seen from flat surfaces like those used for parallel-plate transmission lines.

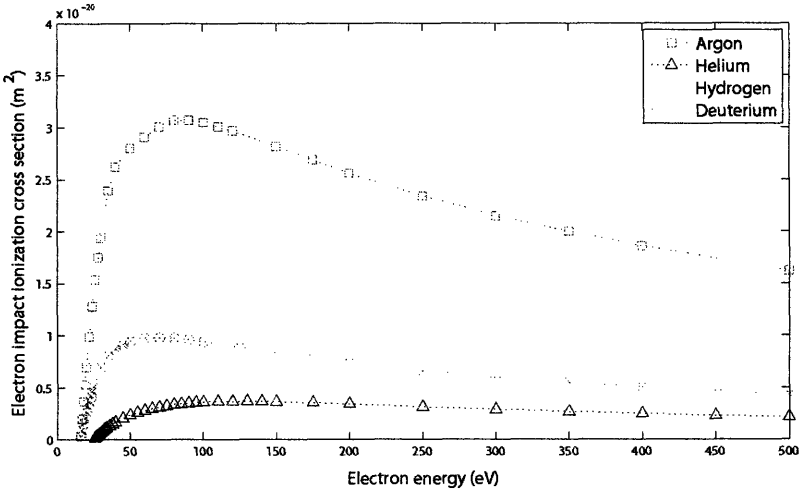

Figure 4.6: Cross sections for electron-impact ionization of argon [67], helium [68], hydrogen and deuterium [69].

4.2.3 Breakdown of different gases

Multipactor-induced glow onset at pressures an order of magnitude lower than Paschen breakdown has been observed for argon in CMX, and the associated neutral pressure limits have been seen for deuterium in C-Mod, but these limits have not been observed for other gases such as helium. Breakdown studies for argon, helium and hydrogen with and without a magnetic field present were performed on CMX.

The microscopic cross sections for electron-impact ionization, the expected driving mechanism of multipactor-induced gas breakdown, are included in Figure 4.6. Unsurprisingly, the cross sections for hydrogen and deuterium are almost identical, so using the former in the experiments is adequate to model the results for the latter, which is more relevant to toka-

maks.

Obviously, argon is by far the most susceptible gas to ionization by electron impact, followed by hydrogen, while helium is the least likely to undergo breakdown for a given voltage amplitude, assuming that other mechanisms for ion and electron generation or loss are not as significant. This helps to explain why the neutral pressure limits associated with a multipactor-induced glow discharge are not observed with helium. Also, since most of the data presented here were obtained using argon, it is likely that gas in tokamaks is somewhat less susceptible to glow onset than the results here suggest. In particular, it could be possible for surface roughening and cleaning methods that did not suppress the multipactor-induced breakdown of argon are more successful with deuterium.

Figure 4.7 shows the obtained breakdown voltages for the three gases for $B_0 = 0, 100\,\mathrm{G}$ for different pressures. Several runs are displayed for each case. As expected, the larger field generally results in lower onset voltages. The notable exception is helium for low pressures; it was actually very hard or impossible to obtain even a faint glow for pressures below 10 mtorr in the magnetized case. The reason behind this remains to be seen, but those plots also show the upward-curving behavior for higher pressures characteristic of Paschen breakdown curves for pressure above 15 millitorr.

The differences between the three gases is not as clear-cut as expected from the ionization cross-sections. While helium does generally exhibit the higher onset voltages, unmagnetized breakdown thresholds are actually higher for argon than for hydrogen at low pressures, in the range for multipactor-induced breakdown.

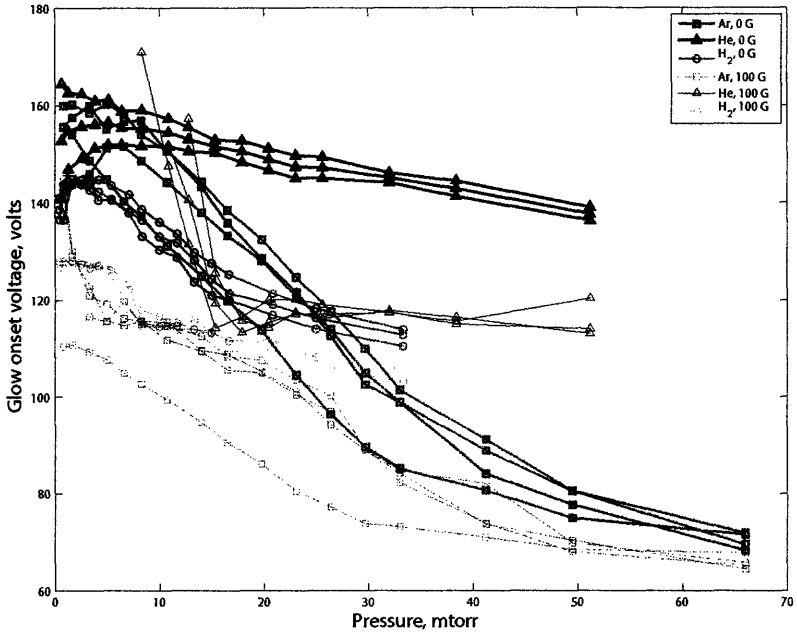

Figure 4.7: Lower boundary breakdown voltages for argon, helium and hydrogen in CMX.

Chapter 5

Monte Carlo simulation

Multipactor physics is fundamentally stochastic, since secondary emission follows characteristic probability distribution functions determining the initial conditions of electrons, as discussed in Section 2.2. Numeric solutions to the appropriate equations of motion that take this randomness into account can thus provide important data that cannot be obtained from CMX or information that helps explain experimental observations. A three-dimensional, particle-tracking simulation applying Monte Carlo sampling techniques, based on the work of Graves [6] and Schmit [63], was upgraded to get such solutions for the regimes of interest for the present study.

5.1 Description

The simulation consists of repeatedly launching an electron from one of the electrodes and tracking its trajectory under external conditions set by the user, until it impacts a surface. Provided it satisfies the condition for multi-

plication, a secondary electron is born from the point of impact and tracked, until one of the subsequent generations fails to produce a new electron. Secondary emission is considered to be instantaneous, since the time scales for the processes described in 2.2 are much shorter than those for electron motion between the electrodes. Each emitted electron has an initial energy and angle selected randomly according to the relevant distribution functions, so a large number of seeded particles is needed for statistically significant results. The simulation runs presented had 4,000 seeded particles, with half of them launched from each electrode, and emitted from sixteen points distributed evenly along each circumference. The code also allows for launch points limited to a single location or to a range of ϕ values.

Two possible options exist for the multiplication condition. The first, following Graves, is using a step function for the secondary electron yield, i.e. $\delta = 1$ for $E_1 < E_p < E_2$, otherwise $\delta = 0$. The present version of the code incorporates the effect of oblique incidence on the yield, so the crossover energies are functions of the angle of incidence. The second possibility is using the full curve to evaluate the yield for each electron impact, in order to include effects like electron population growth. A more sophisticated code would emit zero or more electrons according to a discrete distribution function such like those discussed in Section 2.2.4, with an expectation equal to δ. However, this would require more seeded electrons due to the extra randomly sampled variable, and it would lead to many more particles being tracked, especially for later generations, so it would be very demanding computationally. Instead, this code allows the option to get only one new electron per hit for any $\delta > 0$, i.e. $E_p > E_0$, and assigns a weight W_i to the electron of

the i^{th} generation given by the product of all the δ values for the hits by the electrons of the previous generations, as evaluated using the full yield curve:

$$W_i \equiv \prod_{j=1}^{i-1} \delta_j(E_{p,j}, \theta_j). \tag{5.1}$$

The weights can then be applied to the data obtained to get an admittedly rough idea about population growth and information about the evolution of multipactor physics with time.

Particle trajectories are tracked using a two-step iterative Euler relaxation method, with 100,000 time steps per RF period. Equations 3.18-3.20 and the initial values of r, ϕ and z and their time derivatives at each step are used to obtain rough approximations of the time derivatives at the end of the step. These estimates and the initial derivatives are averaged and used to calculate approximate end-of-step position coordinates. Repeated averaging with initial values and recalculation leads to adjusted final values, until the variables stabilize sufficiently, and initial conditions for the following step are stored. The code only saves the coordinates every twentieth time step, and uses these data for sample trajectory plots and path length calculations.

5.1.1 External parameters

The code allows the user to control certain external parameters that can simulate the conditions under which the electrons move between the conductors of a vacuum section of a coaxial transmission line. The geometry is specified by the inner and outer electrode radii, a and b, or by one of these and the line's characteristic impedance (to which the other dimension is related by

Equation 2.15). The latter is usually preferable for practical reasons, and the simulation runs for this work were performed in a $50\,\Omega$ configuration, like in CMX, where the line's impedance is designed to match the source's.

The electromagnetic fields can also be specified externally by choosing the DC magnetic field magnitude and the RF voltage amplitude and frequency. The simulations were run with set values of $V_0 = 250\,\mathrm{V}$ and $f = 70\,\mathrm{MHz}$, while B_0 is varied from 0 to 1000 G (0.1 T). The emission phase for the seeded electrodes can also be selected or randomly distributed, but the results presented here were obtained from runs with $\omega t_0 = 0$ and π (provided a field $E_r = -\frac{E_0}{r}\sin\omega t$) for electrons launched from the inner and outer electrodes, respectively. These are somewhat arbitrary, but chosen so that there are favorable conditions for a multipactor discharge.

The model for the secondary emission yield is also decided externally by the user. In this code, it is modeled using Vaughan's empirical formulas in Equations 2.18–2.20, with the default unity values for k_{se} and $k_{s\delta}$, assuming smooth surfaces. The selected values for maximum delta and the corresponding primary energy for normal incidence depends on the material, and would presumably lie somewhere between the values for clean copper and copper oxide (Cu_2O_3) for the CMX setup, since it has copper electrodes with an oxide layer. According to Dionne, $E_{\max}$ is entirely dependent on the bulk properties, while the first crossover energy E_1, whose value is determined from $\delta_{\max}$, depends strongly on surface properties [70]. The values of choice would then be somewhat closer to that of copper for the former and to that of copper oxide for the latter. Considering the figures in the literature shown in Table 2.1, reasonable values are $E_{\max} = 500\,\mathrm{eV}$ and $\delta_{\max} = 1.5$. These are ar-

bitrary, but since the actual numbers are inevitably very sample-dependent, they are as good as any other choices in their vicinities, as well as simple.

5.1.2 Sampling

For every emitted electron, three variables must be randomly sampled to fully determine its initial velocity. Its emission energy specifies its magnitude, while the emission angle relative to the normal to the surface and the angle of the projected vector on the plane of the surface determine its direction. The last one obeys a continuous uniform distribution, so all values between 0 and 2π are equally likely and a common random number generator is used. The other two have more complicated distributions discussed previously, so sampling is performed using cumulative distribution functions.

For a properly normalized probability density function $f(x)$, such that its integral over all possible x equals unity, the cumulative distribution function $F(x)$ is given by:

$$F(x) = \int_{x_{\min}}^{x} f(x')\,\mathrm{d}x', \tag{5.2}$$

for $x_{\min} \leq x \leq x_{\max}$, such that $F(x_{\min}) = 0$ and $F(x_{\max}) = 1$. A number between 0 and 1 is selected with a random number generator, and the value of x corresponding to that value of $F(x)$ is assigned to the variable of interest. The actual distribution will approach the probability density function $f(x)$ as the process is repeated many times.

Chung and Everhart's formulation of the emission energy distribution in Equation 2.16 is used in this simulation. The literature also shows instances of simulations using a Maxwellian distribution instead [45, 57, 71, 72], despite

the experimental evidence against this. The distribution of choice is thus given by:

$$f(E_s) = \frac{E_s}{A(E_s + \Phi)^4}, \tag{5.3}$$

where the normalization constant is $A = \frac{1}{6\Phi^2} - \frac{1}{2(E_c+\Phi)^2} + \frac{\Phi}{3(E_c+\Phi)^3}$, for work function $\Phi = 4.46\,\text{eV}$ corresponding to copper, and cutoff energy E_c. This maximum emission energy is set to the smallest of the primary energy and 50 eV, the traditional cutoff for secondaries. The cumulative distribution function is

$$F(E_s) = \frac{1}{A}\left[\frac{1}{6\Phi^2} - \frac{1}{2(E_s + \Phi)^2} + \frac{\Phi}{3(E_s + \Phi)^3}\right], \tag{5.4}$$

for $0 \leq E_s \leq E_c$.

As discussed in Section 2.2.2, the distribution of the emission angle with respect to the normal to the surface can be modeled as a cosine function independent of the primary energy, so $f(\theta_s) = \cos\theta_s$ and $F(\theta_s) = \sin\theta_s$, for $0 \leq \theta_s \leq \pi/2$.

5.1.3 Outputs

The simulation outputs include sample electron trajectories, energy and secondary yield distributions, mean quantities such as path length and time of flight, and electron population evolution over the first five periods, among other data.

The electron trajectories are shown in a 3-D plot for each run, showing paths in different colors depending on the secondary emission yield corresponding to the electron's impact energy and angle of incidence. Blue paths

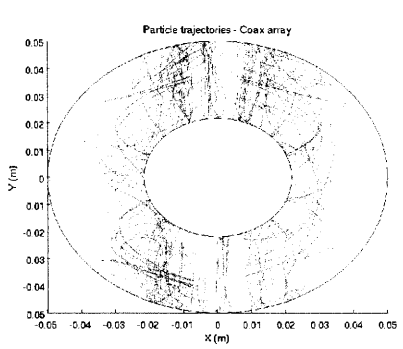

(a) x–y view

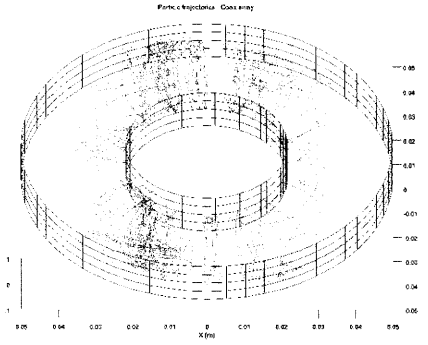

(b) Tilted view

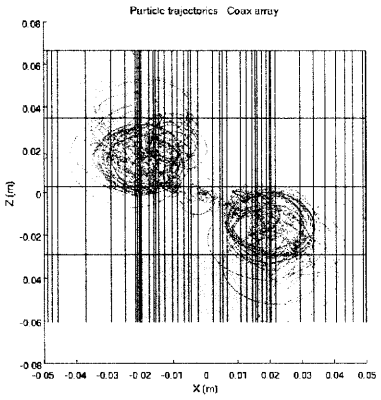

(c) x–z view

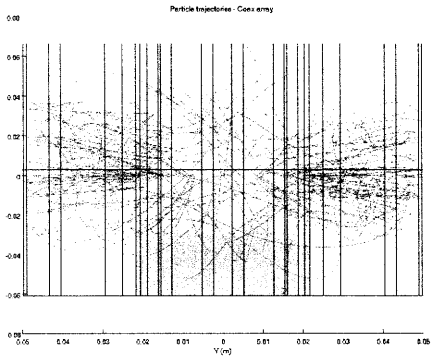

(d) y–z view

Figure 5.1: Simulation trajectory outputs from different perspectives.

have $\delta < 1$, so they lead to overall electron loss. Green and red paths have $\delta > 1$, leading to particle multiplication; for normal incidence, the lower energy threshold E_1 is approximately 125 eV. Red paths correspond to electron in the higher end of the yield spectrum, with $\delta > 1.25$. This cutoff is arbitrarily chosen to be halfway between unity and $\delta_{\max}(\theta = 0)$, and has no special physical significance, but gives additional qualitative information about which trajectories lead to substantial secondary electron emission, contributing most to the development of the discharge.

Figure 5.1 shows sample trajectory plots of the same run from different perspectives. The x–y view is usually the most useful since all fields lie on that plane, but the other views also help to get an idea of displacement in the axial coordinate z, or of the size of the gyroradius of the Larmor motion induced by the **B**-field along y, as shown in panel (c) for the x–z view.

5.2 Results

5.2.1 Electron trajectories

Figures 5.2 and 5.3 show sample electron trajectories in the x–y plane view for five different magnetic field strengths. The seeded electrons are launched from the inner electrode in the plots on the left, while seeded particles on the right are emitted from the outer electrode, with an RF phase $\omega t_0 = \pi$. These are displayed separately for clarity. In each case, five electrons are ejected from each of the sixteen launch points, and subsequent generations are also tracked.

The dependence of the electron trajectory characteristics on B_0 falls

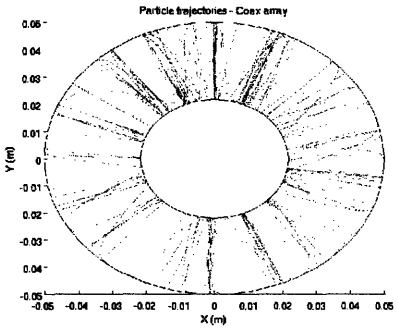

(a) $B_0 = 0\,\mathrm{G}$, inner seeding

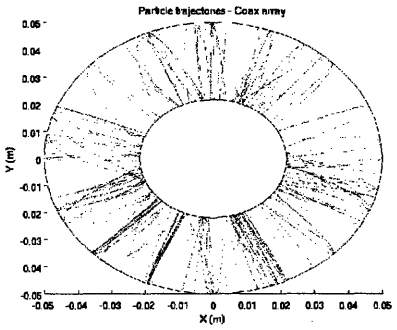

(b) $B_0 = 0\,\mathrm{G}$, outer seeding

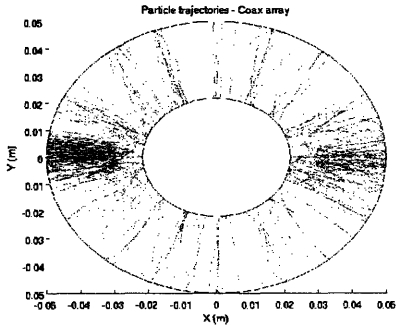

(c) $B_0 = 15\,\mathrm{G}$, inner seeding

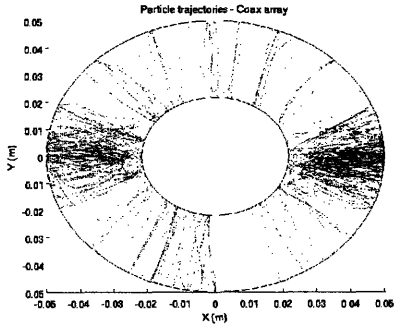

(d) $B_0 = 15\,\mathrm{G}$, outer seeding

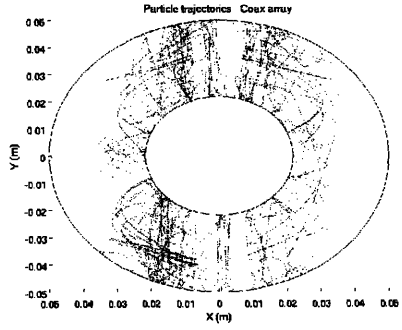

(e) $B_0 = 30\,\mathrm{G}$, inner seeding

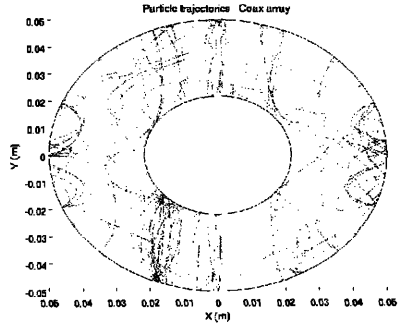

(f) $B_0 = 30\,\mathrm{G}$, outer seeding

Figure 5.2: Sample electron trajectories. Electrons seeded from the inner electrode on the left, from the outer electrode on the right.

roughly into five broad regimes:

1. For zero or very low magnetic field, the electric field dominates and forces are, in essence, purely radial. Hence, all acceleration is in $\hat{\mathbf{r}}$, with all azimuthal or axial motion due to the electron's initial conditions upon being emitted. Electron impacts on the walls are distributed evenly around the circumference.

2. For B_0 in the order of a few gauss, the magnetic force starts to compete with the electric one. For $\phi \approx \pm\pi/2$, the component of the velocity $v_\perp$ is small, so the $\mathbf{v} \times \mathbf{B}$ term is usually not large enough to affect the motion dominated by the electric field; this gradually changes as ϕ gets closer to $0, \pi$. For these regions, the magnetic force is considerable at these field strengths, but not nearly large enough to constrain particle trajectories tightly around the magnetic field lines. Instead, electrons are very loosely contained, with some large-gyroradius Larmor motion superimposed to the radial motion due to the electric field. This weak effect thus adds a transverse component to the particle trajectories in this region, leading to a degree of concentration of the electron paths around the $y = 0$ plane, as seen for $B_0 = 15\,\mathrm{G}$ in panels (c) and (d) of Figure 5.2.

3. For stronger fields of magnitude $\sim 30\,\mathrm{G}$, motion becomes very chaotic overall, as seen in panels (e) and (f) of Figure 5.2. The magnetic force is now strong enough to compete fully with the electric field. In particular, the gyroradius is now in the order of the electrode separation distance $d = b - a$, so many electrons emitted in the regions where $\phi \approx$

$0, \pi$ cannot reach the opposite electrode, as the plots show, especially for those ejected from the inner conductor.

4. Magnetic fields start to dominate strongly for strengths of 50–100 G. Particles are constrained more tightly around the field lines, with gyroradius $r_L \ll d$. There is very little variation in x, so only particles emitted with $|x_0| \lesssim a$ can reach the opposite electrode. Panels (a) and (b) of Figure 5.3 illustrates this case for 100 G.

5. In the kilogauss range, the magnetic field dominates completely and electron trajectories are bound very tightly by the field lines. The gyroradius is practically negligible and the electric field only drives the parallel motion of the particles. Any further increase in B_0 has essentially no effect on the single-particle motion, but can affect collective phenomena.

The plots in Figure 5.4 show the effect of different magnetic field strengths on the characteristics of the particle trajectories. Panels (a) and (b) confirm the main properties of electron paths in the regimes discussed. The mean absolute change in the axial coordinate z between emission and impact is maximized at around 15 G, in regime 2, due to the extra transverse component of motion induced by the weak magnetic field. This quantity falls for larger fields, as the gyroradius becomes comparable to and then smaller than the electrode separation, corresponding to the regimes where the magnetic field prevails and electrons become much more tightly constrained by the field lines.

The quantity $\zeta \equiv \langle \sin^2 \phi_{\text{hit}} \rangle$ shown in panel (b) illustrates the degree

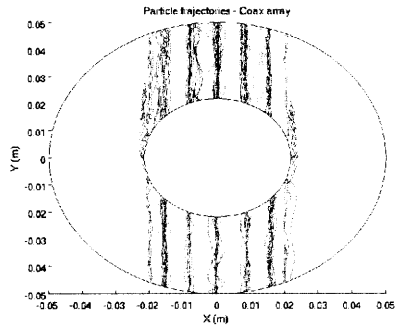

(a) $B_0 = 100\,\mathrm{G}$, inner seeding

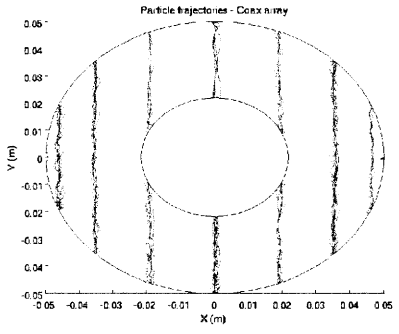

(b) $B_0 = 100\,\mathrm{G}$, outer seeding

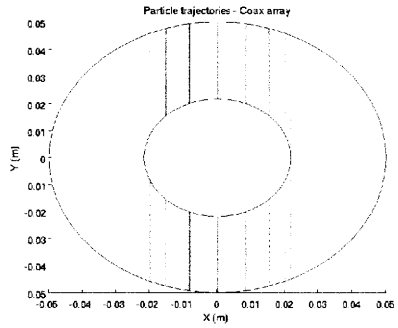

(c) $B_0 = 1000\,\mathrm{G}$, inner seeding

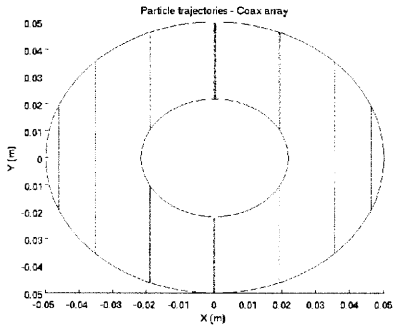

(d) $B_0 = 1000\,\mathrm{G}$, outer seeding

Figure 5.3: Sample electron trajectories. Electrons seeded from the inner electrode on the left, from the outer electrode on the right.

to which electrons are deviated from radial motion by the magnetic field in the x–y plane. Deflections toward the $y = 0$ plane correspond to values closer to zero; those toward the $x = 0$ plane, to values closer to unity. Since the seeded electrons are emitted at evenly spaced points in the azimuthal coordinate ϕ, the unmagnetized case corresponds to near-radial motion and $\zeta \approx 0.5$. As discussed before, a weak magnetic field leads to a concentration of the trajectories near the $y = 0$ plane due to the induced transverse motion near that plane, leading to a decrease in ζ to a minimum in regime 2. Higher fields constrain the electrons around the field lines, leading to deflections toward the $x = 0$ plane and an increase in ζ to 0.7–0.8 for large values of B_0. There is little change in this parameter beyond ~ 75 G, as the magnetic force dominates.

Panels (c) and (d) show that both the mean distance traveled and mean time between emission and impact reach maxima at fields below 50 gauss, between regimes 2 and 3, and decrease for higher fields to a roughly constant level. At these strengths, most electrons follow longer, more complicated paths, unlike the limits of low and high B_0, for which trajectories are largely straight along r and y, respectively.

The mean path length and flight time for the unmagnetized case and that of tokamak-relevant field strengths are not significantly different and cannot account for the observed differences in the effects of multipactor discharges on ICRF antennas between these two limits.

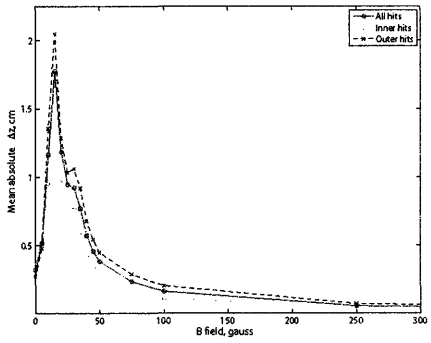

(a) Mean $|\Delta z|$

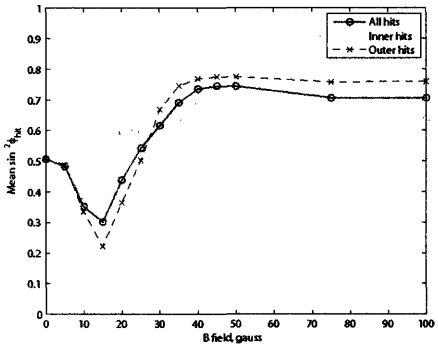

(b) Mean $\sin^2 \phi_{\text{hit}}$

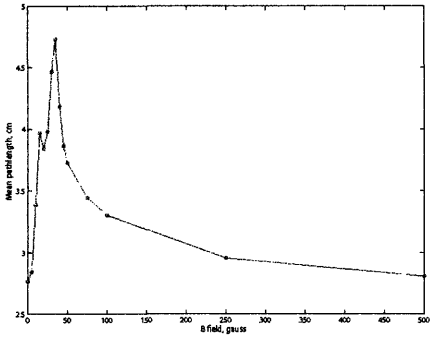

(c) Mean path length

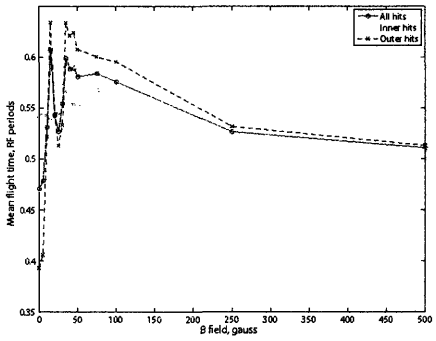

(d) Mean flight time

Figure 5.4: Effect of magnetic field on trajectory characteristics.

5.2.2 Primary impact and secondary emission

In the absence of a magnetic field, most primary electron impacts are close to normal to the surface, since the only force is radial and secondary electrons are emitted at an angle with a (preferentially radial) cosine distribution. The introduction of a magnetic field makes oblique incidence more likely as Larmor motion is induced, which affects the secondary emission yield curve as discussed in Section 2.2.3.

As seen in panel (a) of Figure 5.5, the mean angle of incidence is close to 11° in the unmagnetized clade, and it increases in regimes 2 and 3, with a maximum of approximately 33° at a magnetic field strength of around 30 G. The electron gyroradius is of the order of the separation distance, and many particles follow very complex trajectories, increasing the likelihood of incidence at oblique angles. This can be seen in panel (b) clearly, which shows that the incidence angle distribution is broadest in this regime, whereas it is very heavily weighted toward normal incidence in the absence of a magnetic field. Larger values of B_0 correspond to somewhat lower mean angles, with a roughly constant value near 25° for very high fields, which is still over twice that for the unmagnetized case. Using Equation 2.20, one finds that δ_{max} at this angle is approximately 20% larger than that for the mean incidence angle for $B_0 = 0\,\text{G}$, assuming normal smoothness.

However, the most important factor in determining the secondary emission yield for a particular impact is the primary energy, as seen in Figures 5.6 and 5.7. These show the very similar shape of the panel (a) plots of the mean of each quantity for different magnetic field strengths. The peak of the impact energy distribution is essentially constant at around 200 eV, or 80%

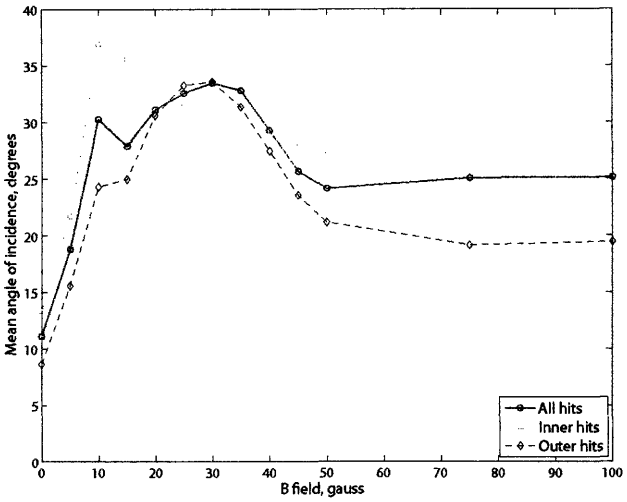

(a) Mean angle of incidence θ

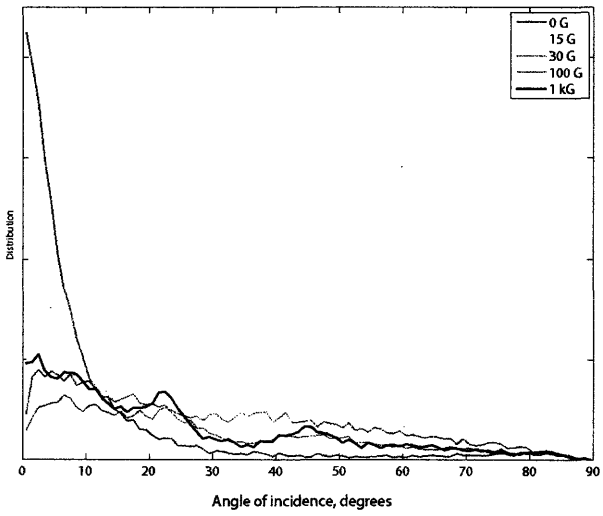

(b) θ distribution

Figure 5.5: Effect of magnetic field on incidence angle.

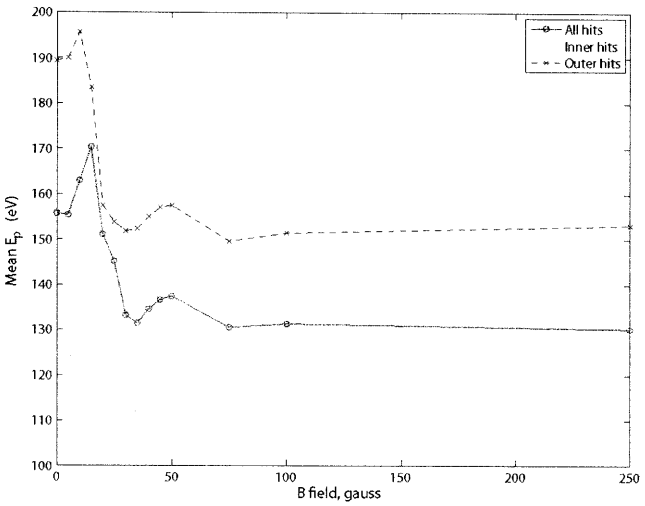

(a) Mean impact energy E_p

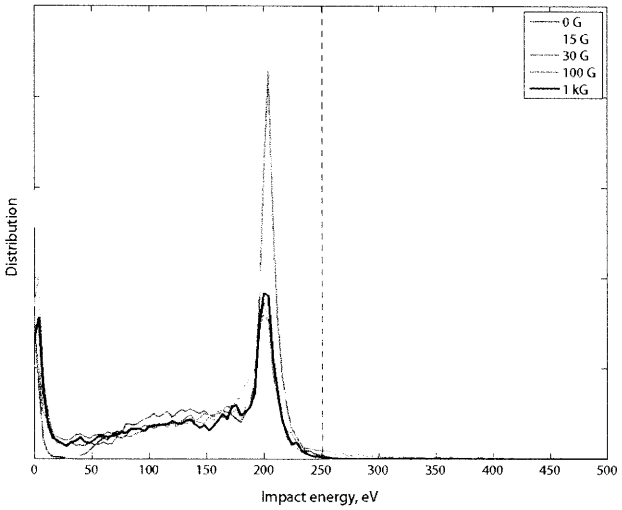

(b) E_p distribution

Figure 5.6: Effect of magnetic field on impact energy.

of eV_0, in agreement with the 1-D simulations for unmagnetized discharges by Graves [6].

While the location of the peak in each of the E_p and δ distributions are practically unchanged by the external magnetic field, the mean quantities are very dependent on B_0. Both reach a maximum in regime 2, at around 15 G, which corresponds to the energy distribution with most high-energy electrons, with the tail dying off at close to 400 eV, rather than just above $eV_0 = 250$ eV for both the low and high field limits. The abundance of higher δ electrons in this regime and, to a lesser extent at $B_0 \approx 30$ G, can be seen in the higher concentration of red trajectories in the plots in Figure 5.2(c)–(f), corresponding to paths with $\delta > 1.25$, the cutoff corresponding almost exactly to the location of all the peaks in the δ distributions.

Both the mean impact energy and secondary yield decay with the magnetic field starting at regime 3, with a mean E_p of about 130 eV (slightly over $0.5eV_0$) and a mean δ between 0.9 and 0.95 for very high fields. The mean yield for tokamak-relevant fields is thus not only below the multiplication threshold, but it is also lower than its no-field equivalent. Again, this does not account for the experimental evidence showing lower onset voltages for the multipactor-induced glow discharge in the presence of a magnetic field.

While the energy distributions show electrons reaching the highest energies in regime 2, the δ distribution shows that higher secondary yields are achieved in regime 3, with the tail dying off at values over 1.7, whereas very few electrons in the 15 G case surpass yields of 1.5. This shows the effect of oblique incidence on δ, as the mean incidence angle is maximized near $B_0 = 30$ G, while it has a local minimum in regime 2, with a mean θ lower

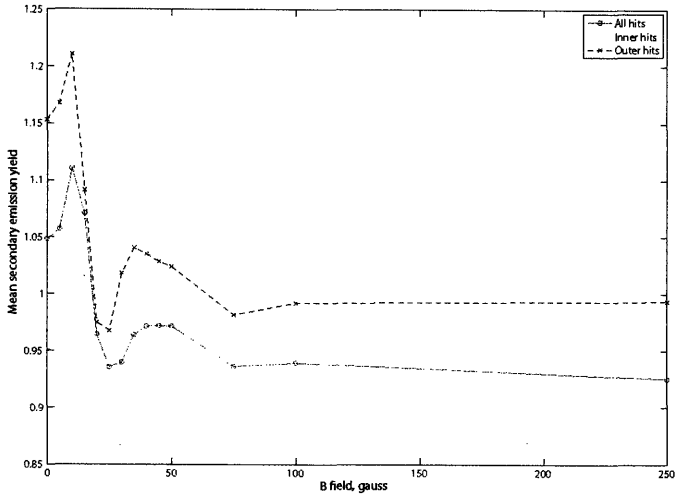

(a) Mean secondary emission yield δ

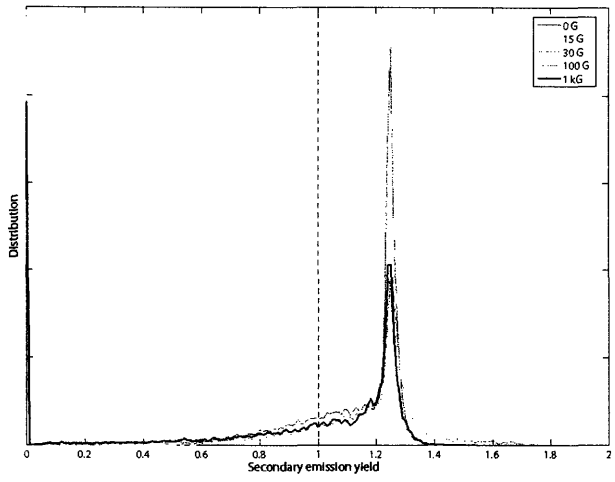

(b) δ distribution

Figure 5.7: Effect of magnetic field on secondary emission yield.

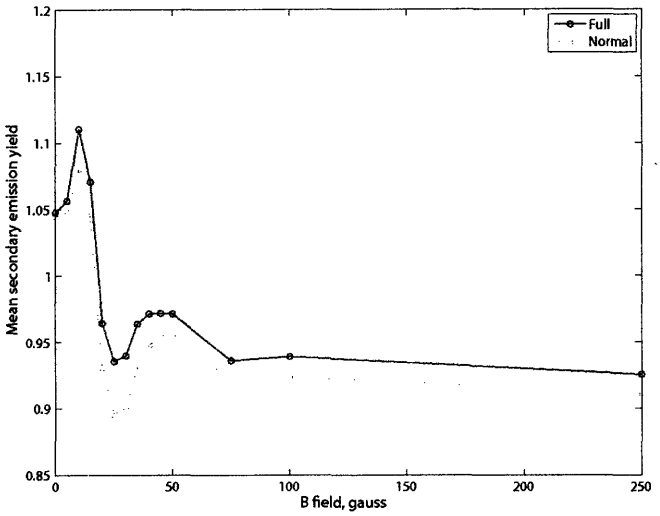

Figure 5.8: Effect of oblique incidence on mean δ.

by about 5°.

Figure 5.7 also shows the effect of oblique incidence on the yield, with mean δ plots using the full θ-dependent and normal incidence expressions from Equations 2.18–2.20. The fractional increase in the mean yield by considering oblique incidence is most important in regime 3, with a 4–5% raise at B_0 =25–30 G; it is a minimum in the unmagnetized case (0.3%), rises rapidly in regime 2 (2.7% at 15 G), and decays to approximately 1.5% for high fields.

5.2.3 Population growth

The effect of the external magnetic field on the electron population evolution can be seen in Figure 5.9. These plots show how the number of particles

between the electrodes changes during the first five RF periods. The cases of electron seeding on the inner and outer conductors are displayed separately since they start at a different time t_0. They are also shown to exhibit very different behavior, unlike in the parallel-plate case, where the two electrodes are geometrically equivalent.

In the unmagnetized case, the growth pattern is very periodic. For inner seeding, a jump in the particle population occurs approximately half a period following the emission of the seeded electrons due to the arrival of many of these to the outer electrode, mostly with secondary yields above unity. This is quickly followed by some of the secondaries emitted before the change in direction of the electric field having too little energy to overcome it, and impacting the same surface with very low or zero δ. The electrons emitted from the outer conductor reaching the inner one do so with a range of yields, mostly between 0.5 and 1.3, resulting in a small increase in the population, followed immediately by a considerable drop from low-energy inner-to-inner trajectories. The number of particle remains roughly constant until roughly the next half-period as a new jump due to the impact of high-δ inner-to-outer electrons, when the cycle starts repeating itself. Some high-yield outer-to-outer electrons, emitted close to one period before, also contribute to multiplication, having followed complicated trajectories and missed the inner electrode altogether due to their angular momentum. A very similar succession of events occurs for the case of outer seeding.

The reason behind the lower mean yield of outer-to-inner electrons relative to that of inner-to-outer ones lies on the more complicated trajectories in the latter case, which leads to a wider spread in the time of flight of the

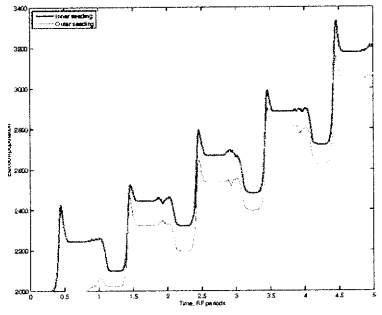

(a) $B_0 = 0\,\mathrm{G}$

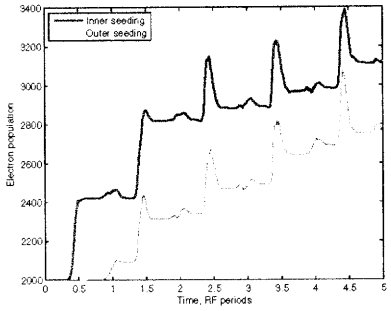

(b) $B_0 = 15\,\mathrm{G}$

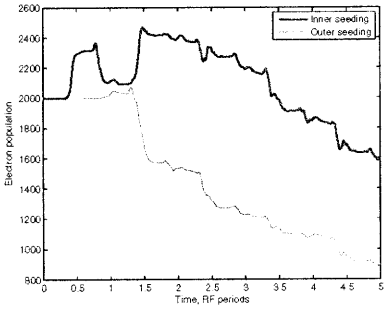

(c) $B_0 = 20\,\mathrm{G}$

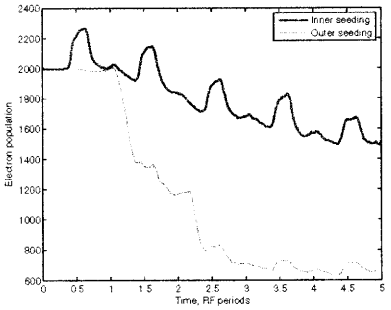

(d) $B_0 = 30\,\mathrm{G}$

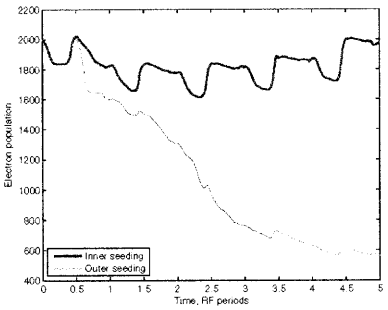

(e) $B_0 = 100\,\mathrm{G}$

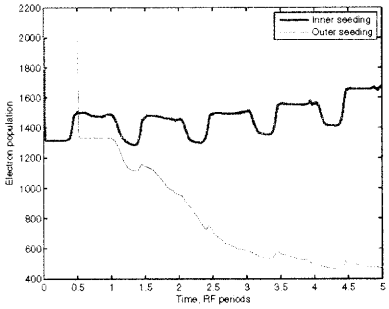

(f) $B_0 = 1000\,\mathrm{G}$

Figure 5.9: Electron population evolution for different magnetic field strengths.

particles. Hence, more of them impact the surface late, as the RF field is changing directions, and are slowed down before they eventually hit with a lower energy and a smaller δ. Also contributing to this, to a lesser extent, is the fact that high-energy electrons launched from the outer conductor can miss the inner one altogether, which is very unlikely in the other direction. These electrons are therefore not included in the comparison, which lowers the mean yield of the outer-to-inner trajectories.

The introduction of a magnetic field makes the succession of events more subtle, disrupting the periodicity of the unmagnetized case. For fields above 15 G, in transition between regimes 2 and 3 or firmly in the latter, there are more electrons hitting the electrode from which they were emitted, many with complex trajectories with durations that do not satisfy the synchronism condition nearly well and do not favor further multiplication by subsequent generations. After some competition between the different mechanisms, there is an overall decay in the number of electrons. This is especially true for outer seeding, which does not count with the initial large jump in population due to inner-to-outer electrons.

For regimes 4 and 5, inner and outer seeding cases exhibit very different behaviors, since the former consists of electrons confined to paths of order $d = b-a$, where outer-to-outer paths are almost necessarily low-energy, while the latter involves both trajectories of order d and, for $|x_0| > a$, outer-to-outer paths only of length scales varying from zero to $\sim 2d$. The frequency and dimensions of the coaxial line show good resonance for trajectories of order d in the unmagnetized case, so many of the very short and very long paths for outer seeding in these regimes are bound to be very unsuitable

for consistent electron multiplication, thus contributing to overall population loss. For inner seeding, resonance can still be somewhat good, despite the fact that only the y-component of the electric field drives their motion parallel to $\mathbf{B}$. Also, transverse disturbances due to weak magnetic fields are no longer an issue, so there can still be growth over several cycles, especially as later generations are more dominated by the paths that yield more multiplication. However, there is significant loss of electrons almost immediately after the initial launch, as the emission energy of many will be mostly directed transverse to the strong magnetic field, so the induced gyromotion is likely to return them to the inner electrode with very low energy, and small or zero yield.

These results do not show any significant advantage for electron population growth in the high-field cases over the unmagnetized scenario, and they even favor growth rates in the latter case. This does not explain the observations in the experiments of greater susceptibility to multipactor-induced glow discharges in the presence of tokamak-scale magnetic fields. The simulation has, however, important weaknesses that are discussed in the following section.

5.2.4 Limitations

The present code suffers from some limitations which must be taken into account when interpreting the results at hand. First, it does not take any collective effects into account. In particular, space charge effects, the defocusing mechanism most responsible for saturation, are not included. This is not necessarily a problem since the simulation only runs for slightly above five

RF periods: electron densities this early in the development of the discharge are almost always too low for any space charge effects to be significant. The short duration of the simulation is, nevertheless, an important weakness on its own. The results only give averaged and time-resolved information for the first few periods of a phenomenon that takes much longer to develop. The three-dimensional nature of the particle-tracking, the use of a full $\delta(E_p, \theta)$ curve and, when relevant (such as for studying population trends), weights for individual trajectories, made the code very demanding computationally, which prevented it to be used for over five periods.

Moreover, the simulation sometimes suffers from being too discrete. In particular, for very high-fields, each trajectory has practically constant x coordinates, so the discreteness in the location of the initial seeding (sixteen points evenly spaced around each circumference) means that the paths under study are very restricted. For small B_0, at least subsequent generations can start at values of x_0, since the primaries are more free to follow more interesting trajectories, but this is not the case for high magnetic fields. Many paths with better (or worse) resonance with the geometry and frequency are thus ignored completely in this limit, which can contribute to change the growth rates and other characteristics of the process. Something similar can be said of the initial seeding at either $\omega t_0 = 0$ or π only. In each case, either more of these discrete alternatives or a sampling process of a continuous range of values could be used to take new trajectories into account, but such approaches would require larger numbers of particles for any results to be representative, which would lead to more computationally-intensive simulations.

Chapter 6

Conclusions

The results from this work lead to several important conclusions about the way coaxial multipactor discharges work and how they are affected by the presence of a strong, constant and uniform magnetic field, as relevant to operation of ICRF antenna systems for auxiliary plasma heating in the Alcator C-Mod tokamak and other magnetic confinement fusion devices.

Findings

The externally applied magnetic field dramatically affects the particle trajectories, which, broadly speaking, fall into five different regimes as discussed in Section 5.2. The magnetic field reduces the degree of detuning of RF systems by coaxial multipactor discharges in vacuum, as shown by the decrease in the reflected power to the source. This is probably due to the smaller change in impedance as opposite-electrode impact is made less likely by the tight confinement of electrons around the magnetic field lines perpendicular to

the direction of propagation of electromagnetic waves in transmission lines. This decrease in reflected power makes it more difficult to detect multipactor susceptibility in a RF system.

Such a discharge is less likely to be detrimental under vacuum conditions, but induced glow breakdown at low gas pressures can severely affect the performance of antennas, since large magnetic fields are shown to decrease the lower onset voltages and the minimum pressures at which such breakdown occurs. The neutral pressure limits observed in Alcator C-Mod should therefore be worse during magnetized operation.

The simulation results do not show any significant increase in path length, time of flight and energy of electrons at high fields relative to the unmagnetized case, so there does not appear to be increased gas ionization on a per-electron basis at low neutral pressures causing the experimentally observed greater susceptibility to multipactor-induced gas breakdown for higher fields.

Furthermore, these results do not support the possibility of larger mean secondary emission yields and electron population growth in the presence of a strong magnetic field. Hence, the aforementioned observation of larger high-field susceptibility to glow discharge onset cannot, according to these data, be accounted for by larger electron densities due to enhanced secondary electron emission, which could otherwise lead to larger total gas ionization rates and easier breakdown onset.

A stronger possibility is that the strong magnetic field affects the rates of space-charge-induced and collisional diffusion of electrons and ions (initially created by ionization of gas by multipactor electrons) to the walls by strongly constraining them around the field lines, thus preventing diffusion in direc-

tions transverse to the field, and decrease the rate at which charged particles are lost and increases the chance of ionization while these particles remain in the gap. This makes it easier for electron-impact ionization to overcome loss mechanisms and lead to a buildup of a full glow discharge.

Future work

Future work should on this subject should concentrate on creating more robust simulations for the coaxial geometry in the presence of magnetic fields of different strengths. In particular, collective effects such as space-charge defocusing of electrons should be included, as well as interactions with gas molecules, such as ionization, attachment and collisional diffusion. Such an endeavor would likely be a long-term project and needs to take into account the limitations affecting the current code, trying to reach a balance between computational efficiency and realistic simulation of conditions.

Experimentally, the focus should be on multipactor avoidance, looking into other sequences and methods of surface roughening and in-situ cleaning processes. There is no apparent reason why treating both the inner and outer conductors could not fully suppress multipactor discharges, except for the problems with the deposition of impurities from other materials on the electrode surfaces during cleaning due to the low vacuum conductance of the coaxial configuration. Also, the increase in secondary yields due to oblique incidence, of greater importance for magnetized systems should not be significant for rough surfaces, and roughening surface treatments on both electrodes have already been shown to suppress multipactor in the parallel-plate

geometry configuration of CMX.

Bibliography

[1] J.R.M. Vaughan. Multipactor. *IEEE Transactions on Electron Devices*, 35(7):1172–1180, 1988.

[2] R. Kishek et al. Multipactor discharge on metals and dielectrics: Historical review and recent theories. *Physics of Plasmas*, 5(5):2120–2126, 1998.

[3] T.P. Graves et al. Effect of multipactor discharge on Alcator C-Mod ion cyclotron range of frequency heating. *Journal of Vacuum Science and Technology A: Vacuum, Surfaces and Films*, 24(3):512–516, 2006.

[4] ITER Physics Expert Group on Energetic Particles, Heating and Current Drive et al. Plasma auxiliary heating and current drive. *Nuc. Fusion*, 39(12):2495–2539, 1999.

[5] T.H. Stix. *Waves in Plasmas.* Springer, 1992.

[6] T.P. Graves. *Experimental Investigation of Electron Multipactor Discharges at Very High Frequency.* PhD thesis, Massachusetts Institute of Technology, 2006.

[7] S.J. Wukitch et al. Investigation of performance limiting phenomena in a variable phase ICRF antenna in Alcator C-Mod. *Plasma Physics and Controlled Fusion*, 46(9):1479–1491, 2004.

[8] A.E. Kadyshevich. The velocity distribution of secondary electrons for various emitters. *Journal of Physics - USSR*, 9:431–435, 1945.

[9] M.S. Chung and T.E. Everhart. Simple calculation of energy distribution of low-energy secondary electrons emitted from metals under electron bombardment. *Journal of Applied Physics*, 45:707–709, 1974.

[10] H. Bruining. *Physics and Applications of Secondary Electron Emission.* Pergamon Press, 1954.

[11] D.J. Gibbons. Secondary electron emission. In A.H. Beck, editor, *Handbook of Vacuum Physics*, volume 2. Pergamon Press, 1966.

[12] K.G. McKay. Total Secondary Electron Emission from Thin Films of Sodium on Tungsten. *Physical Review*, 61:708–713, 1942.

[13] H. Seiler. Secondary electron emission in the scanning electron microscope. *Journal of Applied Physics*, 54(11):R1–R18, 1983.

[14] I. Bojko, N. Hilleret, and C. Scheuerlein. Influence of air exposures and thermal treatments on the secondary electron yield of copper. *Journal of Vacuum Science and Technology A: Vacuum, Surfaces and Films*, 18(3):972–979, 2000.

[15] N.R. Whetten. A review of experimental methods in the field of secondary electron emission, 1961. General Electric Research Laboratory Report No. 61-RL-2733 E.

[16] D. Ruzic et al. Secondary electron yields of carbon-coated and polished stainless steel. *Journal of Vacuum Science and Technology*, 20(4):1313–1316, 1982.

[17] V. Baglin et al. The secondary electron yield of technical materials and its variation with surface treatments. In *Proceedings of the 7th European Particle Accelerator Conference*, Vienna, Austria, 2000.

[18] B.K. Agarwal. Variation of Secondary Emission with Primary Electron Energy. *Proceedings of the Physical Society*, 71:851–852, 1958.

[19] E.M. Baroody. A Theory of Secondary Electron Emission from Metals. *Physical Review*, 78:780–787, 1950.

[20] A.E. Kadyschewitsch. Theorie der Sekundärelektronenemission aus Metallen. *Journal of Physics - USSR*, 2:115–129, 1940. (In German).

[21] R.G. Lye and A.J. Dekker. Theory of secondary emission. *IEEE Transactions on Electron Devices*, 107:977–981, 1957.

[22] J.R.M. Vaughan. A new formula for secondary emission yield. *IEEE Transactions on Electron Devices*, 36(2):1963–1967, 1989. The formulation presented here was later revised in [23], following the experimental results by Shih and Hor [28].

[23] J.R.M. Vaughan. Secondary emission formulas. *IEEE Transactions on Electron Devices*, 40(4):830, 1993.

[24] H.E. Farnsworth. Electronic Bombardment of Metal Surfaces. *Physical Review*, 25(1):41–57, 1925.

[25] H.O. Müller. Die Abhängigkeit der Sekundärenelektronenemission einiger Metalle vom Einfallswinkel des primären Kathodenstrahls. *Zeitschrift für Physik*, 104:475, 1937. (In German.).

[26] R.E. Kirby and F.K. King. Secondary electron emission yields from PEP-II accelerator materials. *Nuclear Instruments and Methods in Physics Research A*, 469:1–12, 2001.

[27] I.M. Bronshtein and V.A. Dolinin. The secondary electron emission (SEE) of solids at large angles of incidence of primary beam. *Soviet Physics - Solid State*, 9(9):2133–40, 1968.

[28] A. Shih and C. Hor. Secondary emission properties as a function of the electron incidence angle. *IEEE Transactions on Electron Devices*, 40(4):824–829, 1993.

[29] H. Bruining. The depth at which secondary electrons are liberated. *Physica*, 3(9):1046–1052, 1936.

[30] D. Vender, H.B. Smith, and R.W. Boswell. Simulations of multipactor-assisted breakdown in radio frequency plasmas. *Journal of Applied Physics*, 80(8):4292–4298, 1996.

[31] Yu.A. Filippov. Statistics of secondary electron emission for nickel and iron. *Soviet Physics - Solid State*, 8(3):701–705, 1966.

[32] V.Y. Foo and R.C. Dougal. Multiple emission distribution of secondary electrons from metals. *Journal of Physics C: Solid State Physics*, 2(1):1324–1331, 1968.

[33] M. Ziegler. Shot effect of secondary emission. *Physica*, 3(1):1–11 and 3(7):307–316, 1936.

[34] M.A. Furman and M.T.F. Pivi. Probabilistic model for the simulation of secondary electron emission. *Physical Review Special Topics - Accelerators and Beams*, 5(12):124404, 2002.

[35] I. Cohen, R. Golan, and S.R. Rotman. Applying branching processes theory for building a statistical model for schanning electron microscope signals. *Optical Engineering*, 39(1):254–259, 2000.

[36] T. Koshikawa and R. Shimizu. A Monte Carlo calculation of low-energy secondary electron emission from metals. *Journal of Physics D: Applied Physics*, 7:1303–1315, 1974.

[37] K. Kanaya and H. Kawakatsu. Secondary electron emission due to primary and backscattered electrons. *Journal of Physics D: Applied Physics*, 5:1727–1742, 1972.

[38] V.P. Gopinath, J.P. Verboncoeur, and C.K. Birdsall. Multipactor electron discharge physics using an improved secondary emission model. *Physics of Plasmas*, 5(5):1535–1540, 1998.

[39] W. Henneberg, R. Orthuber, and E. Steudel. Zur Wirkungsweise des Elektronenvervielfachers I. *Zeitschrift für technische Physik*, 4:115–120, 1936. (In German.).

[40] E.W.B. Gill and A. von Engel. Starting Potentials of High-Frequency Gas Discharges at Low Pressure. *Proceedings of the Royal Society of London. Series A, Mathematical and Physical Sciences*, 192(1030):446–463, 1948.

[41] A.J. Hatch and H.B. Williams. The Secondary Electron Resonance Mechanism of Low-Pressure High-Frequency Gas Breakdown. *Journal of Applied Physics*, 25(4):417–423, 1954.

[42] A.J. Hatch and H.B. Williams. Multipacting Modes of High-Frequency Gaseous Breakdown. *The Physical Review*, 112(3):681–685, 1958.

[43] S.C. Brown. *Basic Data of Plasma Physics*. MIT Press, 1959.

[44] A.L. Gilardini. New breakdown modes of the multipacting discharge. *Journal of Applied Physics*, 71(9):4629–4631, 1992.

[45] A.L. Gilardini. Multipacting discharges: Constant-k theory and simulation results. *Journal of Applied Physics*, 78(2):783–795, 1995.

[46] A. Miller, H.B. Williams, and O. Theimer. Secondary-Electron-Emission Phase-Angle Distributions in High-Frequency Multipacting Discharges. *Journal of Applied Physics*, 34(6):1673–1679, 1963.

[47] R. Woo and A. Ishimaru. A Similarity Principle for Multipacting Discharges. *Journal of Applied Physics*, 38(13):5240–5244, 1967.

[48] K. Krebs and H. Meerbach. Die Pendelvervielfachung von Sekundärelektronen. *Annalen der Physik*, 6(15):189–206, 1955. (In German.).

[49] S. Riyopoulos, D. Chernin, and D. Dialetis. Theory of electron multipactor in crossed fields. *Physics of Plasmas*, 2(8):3194–3213, 1995.

[50] R. Kishek, T.Y. Lau, and Chernin D. Steady state multipactor and dependence on material properties. *Physics of Plasmas*, 4(3):863–872, 1997.

[51] R. Kishek and Y.Y. Lau. Interaction of Multipactor Discharge and rf Circuit. *Physical Review Letters*, 75(6):1218–1221, 1995.

[52] R. Woo. Multipacting Discharges between Coaxial Discharges. *Journal of Applied Physics*, 39(3):1528–1533, 1968.

[53] R. Woo. Final Report on RF Voltage Breakdown in Coaxial Transmission Lines, 1970. NASA/Jet Propulsion Laboratory Technical Report 32-1500.

[54] R. Udiljak et al. Multipactor in a coaxial transmission line. I. Analytical study. *Physics of Plasmas*, 14(3):033508, 2007.

[55] A.M. Pérez et al. Nuevo modelo riguroso para la predicción del efecto multipactor en guía coaxial. In *Proceedings of the XX URSI National Symposium*, Gandía, Spain, 2005. (In Spanish).

[56] E. Somersalo, P. Ylä-Oijala, and D. Proch. Analysis of multipacting in coaxial lines. In *Proceedings of the 1995 Particle Accelerator Conference*, Dallas, TX, 1995.

[57] V.E. Semenov et al. Multipactor in a coaxial transmission line. II. Particle-in-cell simulations. *Physics of Plasmas*, 14(3):033509, 2007.

[58] S. Riyopoulos. Multipactor saturation due to space-charge-induced debunching. *Physics of Plasmas*, 4(5):1448–1462, 1997.

[59] S. Deb and N. Goswami. Breakdown in high frequency electrodeless discharge at low pressure in the presence of a steady transverse magnetic field. *British Journal of Applied Physics*, 15:1501–1509, 1964.

[60] A. Valfells et al. Effects of an external magnetic field, and of oblique radio-frequency electric fields on multipactor discharge on a dielectric. *Physical of Plasmas*, 7(2):750–757, 2000.

[61] R.L. Geng and H.S. Padamsee. Exploring Multipacting Characteristics of a Rectangular Waveguide. In *1999 Particle Accelerator Conference*, New York, NY, 1999.

[62] R.L. Geng et al. Experimental Studies of Electron Multipacting in CESR Type Rectangular Waveguide Couplers. In *8th European Particle Accelerator Conference*, Paris, France, 2002.

[63] P. Schmit et al. *Investigation of Coaxial Multipactor in the Presence of a Magnetic Field.* Poster presentation, 48th Annual Meeting of the APS Division of Plasma Physics, November 2006.

[64] F. Höhn et al. The transition of a multipactor to a low-pressure gas discharge. *Physics of Plasmas*, 4(4):940–944, 1997.

[65] T.P. Graves et al. The Coaxial Multipactor Experiment (CMX): A facility for investigating multipactor discharges. *Review of Scientific Instruments*, 77(1):014701–014704, 2006.

[66] P. Bonanos. Coil Data Compilation (Tech. Memo 207). Princeton Plasma Physics Laboratory, 1964.

[67] J. Fletcher and I.R. Cowling. Electron impact ionization of neon and argon. *Journal of Physics B: Atomic and Molecular Physics*, 6:L2585–L261, 1973.

[68] R.G. Montague, M.F.A. Harrison, and A.C.H. Smith. A measurement of the cross section for ionisation of helium by electron impact using a fast crossed beam technique. *Journal of Physics B: Atomic and Molecular Physics*, 17:3295–3310, 1984.

[69] J. Fletcher and I.R. Cowling. Electron-molecule collision ionization in hydrogen and deuterium. *Journal of Physics B: Atomic and Molecular Physics*, 6:665–674, 1973.

[70] G.F. Dionne. Origin of secondary-electron-emission yield-curve parameters. *Journal of Applied Physics*, 46(8):3347–3351, 1975.

[71] V. Semenov et al. Multipactor suppression in amplitude modulated radio frequency fields. *Plasma Physics*, 8(11):5034–5039, 2001.

[72] A. Dexter and R. Seviour. Rapid generation of multipactor charts by numeirical solution of the phase equation. *Journal of Physics D: Applied Physics*, 38:1383–1389, 2005.